Coordination Chemistry Reviews 361 (2018) 98–119

Contents lists available at ScienceDirect

Coordination Chemistry Reviews

journal homepage: www.elsevier.com/locate/ccr

Review

Photoexcited radical anion super-reductants for solar fuels catalysis

Nathan T. La Porte [a], Jose F. Martinez [a], Subhajyoti Chaudhuri [b], Svante Hedström [c], Victor S. Batista [b], Michael R. Wasielewski [a,*]

[a] Department of Chemistry, Argonne-Northwestern Solar Energy Research Center, and Institute for Sustainability and Energy at Northwestern, Northwestern University, 2145 Sheridan Rd, Evanston, IL 60208, USA
[b] Department of Chemistry, Argonne-Northwestern Solar Energy Research Center, and Yale Energy Sciences Institute, Yale University, 225 Prospect St, New Haven, CT 06520, USA
[c] Department of Physics, AlbaNova University Center, Stockholm University, SE-10691 Stockholm, Sweden

ARTICLE INFO

Article history:
Received 18 December 2017
Received in revised form 22 January 2018
Accepted 23 January 2018

Keywords:
Photoinduced electron transfer
Solar fuels
Ultrafast spectroscopy
Transient absorption
Artificial photosynthesis
Radical anions
CO_2 reduction

ABSTRACT

The catalytic transformation of carbon dioxide into fuels is one of the most important reactions for creating a sustainable, carbon-neutral energy economy. Given that the sun is the only plausible energy source that can accommodate the increased global energy demand without contributing to catastrophic climate change, it makes sense to use solar energy to drive this reaction, ideally using the largest possible portion of the solar spectrum. Over the past several years, we have explored the use of reduced rylenediimide chromophores, which absorb wavelengths ranging into the near-infrared, as strongly reducing photosensitizers capable of photosensitizing Re(diimine)$(CO)_3$L metal centers towards the binding and reduction of CO_2. We have explored the effects of varying the binding geometry, donor–acceptor redox potentials, and excitation wavelength on the kinetics of electron transfer from the reduced rylenediimide to the metal center. So far, we have achieved charge-separated lifetimes in electrocatalytically active complexes of 25 ns when illuminated with near-infrared light, and >250 ns when illuminated with blue light.

Contents

* Corresponding author.
E-mail address: m-wasielewski@northwestern.edu (M.R. Wasielewski).

https://doi.org/10.1016/j.ccr.2018.01.018
0010-8545/

1. Introduction

1.1. Background

As we grapple with an increasingly chaotic climate fueled by rising global temperatures and CO_2 levels, the need for a sustainable, carbon-neutral source of fuels has become more and more apparent [1]. At the same time, global demand for energy is expected to increase over the coming decades, from around 14 TW in 2001 to 27 TW in 2050. The only renewable source of energy available to meet this demand is the light from the Sun [2]. While the efficiency of solar photovoltaic devices continues to improve [3], energy storage densities for electricity are still low compared to the energy stored in the chemical bonds of liquid fuels [2]. Consequently, we and many other researchers have sought to achieve the conversion of solar energy into stored chemical energy, an approach akin to the natural photosynthetic process and commonly referred to as artificial photosynthesis. Artificial photosynthetic systems use as their feedstocks the same inputs as natural photosynthesis, namely water as a source of reducing equivalents and carbon dioxide as the substrate to be reduced.

One of the key challenges in an artificial photosynthetic system is to reduce thermodynamically demanding substrates such as CO_2 using as much of the solar spectrum as possible. Typical electrocatalysts employed to reduce CO_2 function at potentials around −1.5 V vs SCE [4], a potential accessible using metalorganic chromophores that absorb at wavelengths shorter than 550 nm [5–9]. In addition, many of these highly reducing chromophores incorporate non-earth-abundant metals such as Ir [10,11], Pt [12], or Re [13]. There are reports of covalent assemblies of metalorganic chromophores with CO_2 reduction catalysts, the most widely researched of which are the $Ru(bpy)_3$–$Re(bpy)(CO)_3$ assemblies reported by Ishitani and co-workers [14], which achieve photocatalysis at wavelengths <500 nm. There has also been a report of a complex of an Ir^{III}(1-phenylisoquinoline)$_2$(bpy) complex attached to a $Re(bpy)(CO)_3$ catalyst, in which catalysis is achieved upon illumination at 480 nm [15]. Other assemblies that function at slightly longer wavelengths (<600 nm) incorporate zinc or magnesium porphyrins [16] or $Os^{III}(bpy)_3$ [17].

In contrast to metalorganic chromophores, purely organic chromophores that absorb in the visible region do not typically possess the excited-state reducing power required to photosensitize CO_2 reduction catalysts. However, it has been shown that certain organic chromophores, when reduced by one or two electrons, become powerful excited-state super-reductants that absorb long-wavelength visible and even near-infrared light while still exhibiting long enough lifetimes for use in donor–acceptor systems [18]. The use of a pre-reduced chromophore to transfer electrons to a CO_2 reduction catalyst has been previously demonstrated by Neumann and co-workers in a system in which a colorless polyoxometalate is reduced at mild potential in the presence of protons to generate an intensely absorbing chromophore [19]. The polyoxometalate is coordinated to a bimetallic CO_2 reduction catalyst, and photoexcitation of the reduced chromophore results in the transfer of two electrons and two protons to the catalyst, enabling binding and reduction of CO_2.

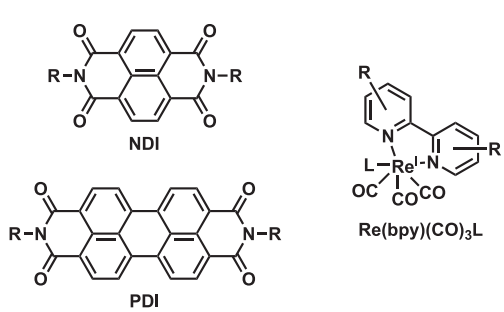

Scheme 1. Structures of naphthalenediimide (NDI), perylenediimide (PDI), and Re(bpy)$(CO)_3$L.

In our work, we have focused on the anions and dianions of rylenediimides (RDIs) as photoreductants. Structures of the rylenediimides used in this work are shown in Scheme 1. RDI anion chromophores were chosen on the basis of their relatively long excited-state lifetimes and the ease with which they can be incorporated synthetically into donor–acceptor assemblies, including metal centers capable of reducing CO_2. Chosen for our initial studies was the prototypical CO_2 reduction catalyst Re(bpy)$(CO)_3$L. This metal center was chosen for several reasons: first, its spectroscopic properties are well-understood, allowing for facile interpretation of our TA data; second, its ligand arrangement allows the chromophore to be attached to the metal center using a variety of geometries, allowing us to explore the effect of geometry on the rate and yield of charge separation; third, there is precedent for photodriving it as a catalyst using a covalently attached chromophore [17,20–24]. Finally, the complex is known to reduce CO_2 through a different set of pathways depending on whether the complex is reduced by one or two electrons before catalysis is initiated [25–28]. This property leaves open the possibility, which we have not yet explored extensively, of attaching multiple chromophores to the metal center and photodriving catalysis via the two-electron pathway.

We will begin this review by describing the properties, determined by ourselves and other groups, of the RDI anions and Re(bpy)$(CO)_3$L complexes, shown in Scheme 1. First we will discuss their ground-state redox (Section 3.1) and optical (Section 3.2) properties. We will then discuss the excited-state spectroscopy of the RDI anions (Section 3.3) and some insights provided by high-level time-dependent density functional theory (TD-DFT) calculations on the excited state properties of PDI radical anion (Section 3.4) before beginning our discussion of RDI–Re(bpy) complexes.

Our initial studies involved direct attachment of the RDI chromophore to the Re(bpy) center, either through the bipyridine ligand, which will be discussed in Section 4.1.1, or through the pyridine ligand, which will be discussed in Section 4.2.1. A second generation of molecules comprised the same attachment geometries but with the addition of an intermediate electron acceptor. This intermediate acceptor was inserted in order to facilitate a longer lifetime of the final charge-separated state without compromising the rate of formation of that state. Those systems are discussed in Section 4.1.2 (bpy-linked) and 4.2.2 (py-linked).

During the course of these studies, we realized that there was also the potential to photodrive these systems in a completely different way, namely by using the Re → bpy MLCT state as the chromophore and the RDI anion as a covalently attached electron donor. The spin dynamics of this pathway proved unexpectedly rich and are discussed in Section 5.

All the systems described in this review have been characterized using electrochemistry to determine the reduction potentials of each moiety, steady-state UV–vis-NIR and mid-IR spectroscopy to establish ground-state optical and vibrational properties, and transient UV–vis-NIR and mid-IR spectroscopy to determine excited-state and electron-transfer dynamics in order to establish the forward- and back-electron transfer rates. In many cases, DFT calculations were employed to explain unexpected behaviors and reveal rich electronic structures. All these studies were performed with an eye towards determining the optimum molecular design for rapid charge separation and slow charge recombination, which would further enable detection of catalytic activity.

1.2. Other developments

The Wasielewski group first investigated the photoexcitation of $NDI^{\cdot-}$ in the context of molecular photoswitches [29,30]. In those reports, $NDI^{\cdot-}$ was generated transiently via excited-state electron transfer from an attached chromophore, and was then excited by a second pump pulse. The excited $NDI^{\cdot-}$ was able to undergo oxidative quenching to transfer an electron to an acceptor that could not have been reduced by the excited state of the first chromophore. While described at the time as a type of molecular photoswitch, the system also resembles a simplified version of the photosynthetic Z scheme, in which a difficult-to-reduce substrate is reduced using visible light photons absorbed by a series of chromophores.

Several other groups have also investigated the use of PDI and NDI anions as highly reducing chromophores. In 2008, Rybtchinski and co-workers reported the preparation of a water-soluble PEG-substituted PDI [31]. Reduction by sodium dithionite produced the water-soluble PDI dianion which was found to be stable in water for months, in contrast to other previously reported aromatic dianions. Due to its stability, it was possible to characterize the dianion by NMR, UV–vis spectroscopy, and time-resolved emission spectroscopy. The Rybtchinski study did not report any applications of the aqueous PDI dianion as a chromophore.

The first report of an application of a PDI anion chromophore was published by König and co-workers in 2014 [32]. In that paper, the authors report the photoreduction of PDI in deaerated DMF or DMSO solution containing Et_3N as a sacrificial reductant. Neutral PDI was found to convert smoothly and quantitatively to the PDI radical anion upon irradiation with 455 nm light. The PDI radical anion was stable under those conditions until air was introduced into the solution. Photocatalytic experiments using 455 nm light were subsequently performed in the presence of a halogenated aromatic electron acceptor, and it was found that aromatic dehalogenation occurred with substrates whose reduction potentials fell below that of the excited state oxidation potential of the PDI radical anion. The authors postulate a Z-scheme-like mechanism in which neutral PDI is excited and reductively quenched by NEt_3 to produce the PDI radical anion. Subsequent excitation of the PDI radical anion results in reduction of the aryl halide to its radical anion, followed by halide loss and reaction of the aryl radical with NEt_3^+ and a solvent molecule to produce the dehalogenated aryl product. Curiously, the reaction mechanism proposed and substantiated through various control experiments implies the photoexcitation of the PDI radical anion by 455 nm light, a wavelength at which the PDI radical anion does not absorb. No explanation is given for this discrepancy.

A follow-up to this work was performed by Duan and co-workers, focusing on improving the solubility of PDI by incorporating it into a Zn-PDI metal–organic polymer [33]. When incorporated into the polymer, the rate and yield of dehalogenation reactions photocatalyzed by PDI in the presence of NEt_3 was improved relative to the homogeneous photocatalysis reported by König and co-workers. The authors suggest that this improvement may be due to the metal–organic polymer preventing aggregation of the neutral PDI species, thereby increasing the rate of electron transfer from NEt_3 to generate $PDI^{\cdot-}$. In addition, immobilizing the PDI chromophore in a heterogeneous polymer simplified the isolation of the dehalogenated product.

Finally, a number of papers have been published by Majima and co-workers exploring covalent assemblies of NDI [34] or PDI [35] chromophores linked through aromatic bridges to various aromatic mono- or diimide acceptors [36]. These assemblies were reduced using either pulse radiolysis in DMF solution [34] or by addition of tetrakis(dimethylamino)ethylene (TDAE) which is able to generate the PDI or NDI radical anion. The rate of electron transfer from the RDI anion was observed to vary based on the driving force for electron transfer, the donor–acceptor distance, and the geometry (*meta* or *para*) of the aromatic bridge. The rates for excited-state electron transfer were found to obey the Marcus relationship and the reorganization energies were derived.

2. Experimental

With the exception of the results presented in Section 5.2, all experimental work discussed in this review has been previously published or is in preparation, and the reader is referred to those manuscripts' experimental sections for details of those experiments. The following computational procedures are applicable to the work presented in Section 5.2.

2.1. Density functional theory methods

All density functional theory (DFT) calculations were performed with the B3LYP exchange–correlation functional [37] and Def2SVP basis set [38]. The Gaussian09 software [39] was used throughout, with "tight" geometry convergence criteria, an "ultrafine" numerical integration grid, and the SMD implicit solvent model [40] of DMF.

The **PDI-Phbpy-Re-Py** dyad (with the solubilizing alkyl chain truncated to a methyl group) was optimized in various electronic states. Closed-shell singlet ground states S0 were calculated with restricted DFT, whereas unrestricted DFT (uDFT) was used for the lowest-energy doublet D0 and triplet states T1. The following states of the dyad were considered: non-reduced ground-state S0 (formally positive due to the Re^{I}), the doubly reduced S0, and doubly reduced T1 (corresponding to the high-spin charge-shifted state). The PDI molecule was similarly optimized in the following electronic states: non-reduced S0, singly reduced D0, doubly reduced S0, and doubly reduced triplet to confirm that the two reducing electrons prefer to pair up in a closed-shell fashion rather than occupy two distinct orbitals in a high-spin manner. The Re(Phbpy)$(CO)_3$Py (**Phbpy-Re-Py**) molecule was optimized in the non-reduced S0, non-reduced T1, and singly reduced D0 states.

Frequency calculations were performed to verify that a structural minimum was reached, and to estimate the thermal contributions to the free energy according to the ideal-gas, rigid-rotor, harmonic-oscillator approximation. The 10 lowest-energy vertical singlet and 10 lowest-energy triplet excited states of PDI^{2-} and **Phbpy-Re-Py** were calculated with linear-response time-dependent (TD) DFT. Computed IR spectra were obtained by applying an arbitrary Gaussian broadening of 6 cm^{-1} FWHM to the calculated IR transitions.

Free energies of each state were computed as the sum of the PDI and **Phbpy-Re-Py** parts. The validity of this fragment approach was verified through thorough testing in a recent study of the same dyad in its singly reduced state [41]. The quantum mechanical interaction between the two parts of the dyad is negligible due to weak coupling, but the classical Coulomb interaction $E_{Coulomb}$

may be significant. The resting and charge-shifted states of the full dyad were optimized, and calculated NBO [42] charges q were fitted to each atom i of **Phbpy-Re-Py** and j of PDI and the pairwise Coulomb interaction was added to the free energy of each dyad state, as estimated according to:

$$E_{\text{Coulomb}} = \sum_{i}^{\text{Re-bpy}} \sum_{j}^{\text{PDI}} \frac{q_i q_j}{4\pi r_{ij} \varepsilon_0 \varepsilon_r}$$

Here r_{ij} is the distance between atoms i and j, and ε_0 and ε_r are the vacuum and DMF (=37.22) relative permittivities, respectively.

3. Properties of RDI and Re(bpy)(CO)$_3$L

3.1. Redox properties

An alluring property of NDI and PDI with respect to the use of their anions as chromophores is the ease with which they can be reversibly reduced [18]. The reduction potential remains fairly invariant despite changes to the substituent on the imide, reflecting the lack of electronic coupling between the RDI core and the imide. Gosztola et al. studied NDI with both 2,5-di-*tert*-butylphenyl and *n*-octyl substituents and found that in both cases, the first reduction occurred at −0.48 V vs SCE, while the second occurred at −0.99 V. The first reduction of PDI was found to occur only slightly more positive of the first reduction of NDI, at −0.43 V vs SCE, while the second reduction was significantly less negative than that of NDI, at −0.70 V. The positive shift in reduction potential as the RDI core is expanded is attributed to the delocalization of the extra electron across a larger aromatic region [43]. In the molecules studied in this study, the distal imide position on the NDI was substituted with 2,5-di-*tert*-butylphenyl, and the distal imide on the PDI was substituted with a tricosan-12-yl group to ensure the solubility of the respective diimides.

The electrochemistry of the Re(bpy)(CO)$_3$L system has been extensively studied [26,28,44]. Briefly, the complex can be reversibly reduced twice under inert atmosphere, with the first reduction, occurring around −1.1 V vs SCE, corresponding to the reduction of the bipyridine ligand from 0 to − 1, and the second, occurring around −1.5 V vs SCE, to the reduction of the Re center from +1 to 0 [28,45]. Varying the substituents on the bpy ligand from electron donating to electron withdrawing can tune its reduction potential over a range of more than 700 mV while having a smaller effect on the reduction of the Re center. Varying the charge on the L ligand from neutral to anionic varies the reduction of the bpy ligand over a smaller range (∼100–200 mV) while having a similar effect on the reduction of the Re center. It has also been observed that in general, better activity as a photo- or electrocatalyst correlates with a more negative potential for the reductions of both the bpy ligand and the Re center, although there are other properties that affect catalytic ability [4,13,44,46]. A discussion of these properties is beyond the scope of this review. In most of the complexes discussed in this review, the bpy ligand was substituted with a phenyl group at the 4 position, as that position proved the easiest to functionalize for incorporation into an extended system.

3.2. Ground-state optical properties

The photophysical properties of the anions of NDI and PDI were first investigated by the Wasielewski group. Shown in Fig. 1 are the spectra of NDI and PDI in their neutral and reduced forms, taken from [47]. The spectra were obtained by chemical reduction of DMF solutions of the neutral compounds using TDAE to produce the radical anions, and cobaltocene to produce PDI^{2-}. These spectra are identical to the spectra obtained by Gosztola et al. using electrochemical reduction of DMF solutions in an optically transparent thin layer electrochemical (OTTLE) cell. Gosztola et al. also collected transient absorption data on the radical anions of NDI and PDI produced by electrochemical reduction in order to determine their excited-state lifetimes. In addition, Rybtchinski and coworkers reduced a water-soluble PDI in aqueous solution with sodium dithionite and determined the lifetime of the PDI dianion by fluorescence lifetime measurement. The results of these various experiments are presented in Table 1. These data allow us to use time-resolved UV–vis-NIR spectroscopy (fsTA and nsTA, for femtosecond-scale and nanosecond-scale spectroscopy, respectively) to determine the excited-state and oxidation state dynamics of complexes containing RDI moieties.

The ground-state UV–visible absorption spectrum of Re(Phbpy)(CO)$_3$L in various oxidation states has been determined by spectroelectrochemical measurement as well and is shown in Fig. 2A below. The singlet cationic molecule contains a broad absorbance centered at 350 nm and tailing into the visible region. This band is assigned by TD-DFT calculations [43] and by analogy to other published Re(bpy)(CO)$_3$L molecules to the Re → bpy MLCT transition [13,48,49]. Upon reduction, a new band arises in the visible region with a maximum around 500 nm whose exact position depends on the substituents on the bpy ligand and the nature of L. This band diminishes to a minimum around 650 nm, and there is also a low-energy band which tails into the infrared [48]. These bands arise from different $\pi^* \rightarrow \pi^*$ transitions in the bpy ligand [50]. While diagnostic of the oxidation state of the Re(bpy) moiety, these bands are weak relative to the RDI bands and are therefore less useful when analyzing the transient data collected on our RDI–Re(bpy) complexes.

More useful for determining the oxidation state and ligand environment of the Re(bpy) moiety is the mid-IR spectrum of the carbonyl stretching region from 1850 to 2050 cm^{-1}. The frequency of these stretches is extremely sensitive to both the oxidation state of the Re center, as expected, but also to the oxidation state of the bpy ligand due to the effect that ligand has on the strength of the π back bonding of the CO ligand. The specific effects of both excitation and redox chemistry on the CO stretching frequencies in Re(bpy)(CO)$_3$L molecules has been extensively reviewed by Ishitani,

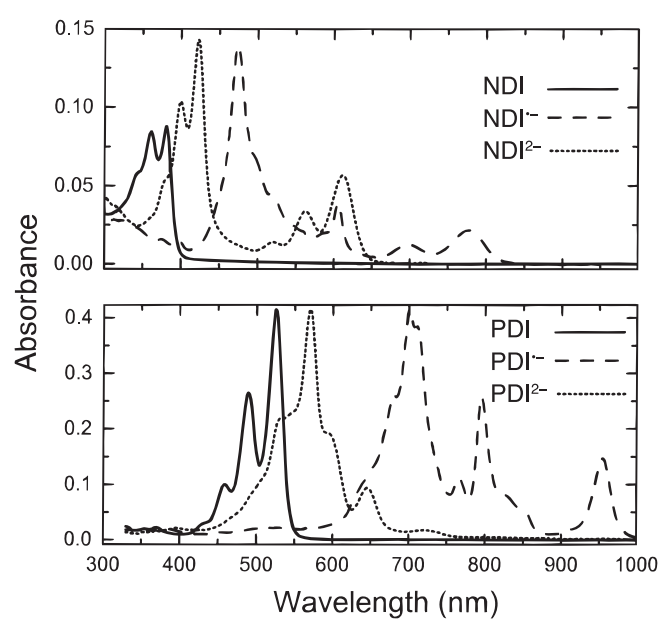

Fig. 1. Ground-state absorption spectra of neutral, radical anion, and dianion forms of **NDI** (top) and **PDI** (bottom) in DMF + Bu_4NPF_6. Adapted and reprinted with permission from [18]. Copyright 2000 American Chemical Society.

Table 1
Photophysical properties of N,N′-bis(2,5-di-*tert*-butylphenyl) **PDI** and **NDI** in the neutral (**N**), radical anion (**R**$^{\cdot-}$), and dianion (**R**$^{2-}$) forms. All data taken from [18] unless noted.

Compound	**N**: λ (nm) (ε (M^{-1} cm^{-1}))	**R**$^{\cdot-}$: λ (nm) (ε (M^{-1} cm^{-1}))	**R**$^{2-}$: λ (nm) (ε (M^{-1} cm^{-1}))	^{1*}**N**: τ (ps)	^{2*}**R**$^{\cdot-}$: τ (ps)	^{1*}**R**$^{2-}$: τ (ps)
NDI	361 (15,100) 381 (16,400)	474 (26,000) 605 (7200) 698 (2400) 777 (4100)	400 (19,500) 423 (26,700) 520 (2600) 563 (6300) 612 (10,600)		141 ± 7	
PDI	458 (19,300) 490 (51,000) 526 (80,000)	680 (50,600) 700 (79,800) 712 (74,200) 766 (21,600) 795 (49,600) 955 (28,200)	532 (42,400) 570 (80,000) 597 (36,700) 646 (18,100) 720 (3400)	3800 ± 100	145 ± 15	6500 [31]

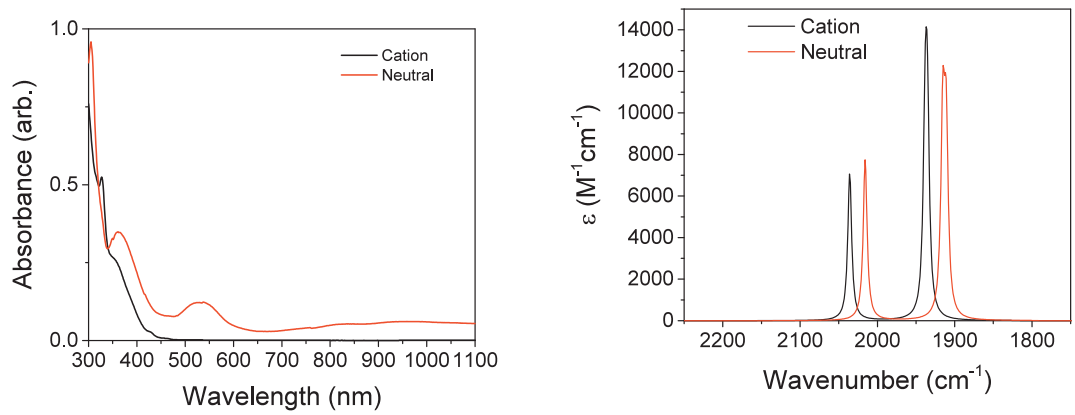

Fig. 2. *Left*: Ground-state absorbance spectra in the UV–vis of cation (Re(I), bpy^0) and neutral (Re(I), bpy$^{\cdot-}$) forms of Re(Phbpy)(CO)$_3$Py in DMF + Bu$_4$NPF$_6$. *Right*: DFT-calculated mid-IR absorbance spectra of Re(Phbpy)(CO)$_3$Py in the cationic and neutral states. Calculated at (B3LYP/Def2SVP(Re), 6-31G*(others)) and scaled by a factor of 0.9671 [51].

Vlček, and co-workers [13,49]. As a consequence, we are able to use time-resolved mid-IR spectroscopy (fsIR) to probe the excited-state and oxidation state behavior of complexes containing Re(bpy)(CO)$_3$ fragments. The advantages of being able to probe this region in a time-resolved manner are the exquisite sensitivity of the CO stretching frequencies to changes to the ligand environment, and the fact that this region is free of any other overlapping absorbances.

Shown in Fig. 3 below are the spectra of two representative RDI–Re(bpy) complexes in their neutral and reduced forms. With the exception of the Re-bpy MLCT absorbance below 450 nm, and the absorbance of oxidized TDAE or CoCp$_2$ below 400 nm, the spectra are practically identical to the spectra of the uncomplexed NDI and PDI molecules shown in Fig. 1. This is indicative of minimal electronic coupling between the RDI and Re(bpy) moieties, a result also borne out by DFT calculations (see Section 3.2). The CO stretches observed in complexes containing both RDI and Re (bpy) moieties are also identical to control complexes containing only the Re(bpy) fragment, as shown in Fig. 2.

3.3. Excited-state spectra of PDI and NDI

The transient spectra of PDI$^{\cdot-}$, PDI^{2-}, and NDI$^{\cdot-}$ are reproduced in Fig. 4 [47]. The radical anion spectra both show very similar features: negative features corresponding to bleaching of the ground state (PDI$^{\cdot-}$: 680 nm, 700 nm, 705 nm, 795 nm, 950 nm; NDI$^{\cdot-}$: 471 nm, 700 nm, 785 nm) and stimulated emission from the excited state (PDI$^{\cdot-}$: 960 nm, 1100 nm, 1300 nm; NDI$^{\cdot-}$: ~800 nm, 900 nm, 1000 nm), and positive features corresponding to induced absorptions from the excited state (PDI$^{\cdot-}$: 470 nm, 525–625 nm; NDI$^{\cdot-}$: <450 nm, 650–675 nm). These features decay simultaneously with the lifetime given in Table 1. The situation with PDI^{2-} is slightly different; the short-wavelength features at λ < 600 nm are due to ground-state bleaching but no stimulated emission features are observed (although the compound is known to be emissive [31]), likely due to overlapping induced absorptions from 600 to 1200 nm. Instead of decaying back to the ground state, however, the singlet excited state produced by photoexcitation converts in several nanoseconds to a different excited state before decaying on the nanosecond timescale.

3.4. Insights from DFT on the ground and excited state manifolds of the PDI radical anion

In order to understand the electronic transitions underlying the PDI radical anion absorbance spectrum, we carried out time-dependent density functional theory (TD-DFT) calculations [47]. The frontier molecular orbitals involved in the electronic transitions in the visible region are shown in Fig. 5. The orbitals are numbered according to their occupancy in neutral PDI, so the LUMO shown is the SOMO of PDI$^{\cdot-}$. All the frontier MOs are observed to be delocalized over the entire PDI core. The vertical (non-vibronic) transitions predicted by TD-DFT are somewhat shorter in wavelength than those observed experimentally, but by calculating the major vibrational modes of the molecule we were able to correct the vertical transition energies to include the vibronic progression of each transition. The calculated energies of the vertical transitions, lowest energies of the vibronically resolved transitions, calculated oscillator strengths, and orbital character of each transition are shown in Table 2. The contributions of each transition to the electronic absorption spectrum are shown in

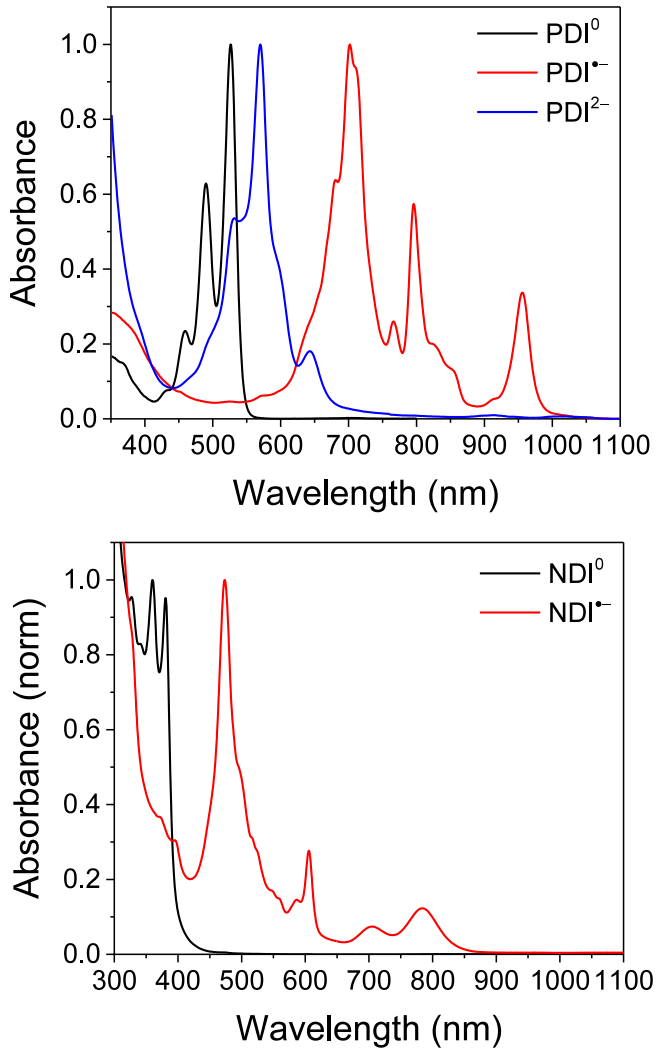

Fig. 3. *Top*: Spectra of **PDI-Phbpy-Re-Py** in the neutral (black), $PDI^{\cdot-}$ (red) and PDI^{2-} (blue) states. *Bottom*: Spectra of **Phbpy-Re-PyPhNDI** in the neutral (black) and $NDI^{\cdot-}$ (red) states. Originally published in [47] by the Royal Society of Chemistry.

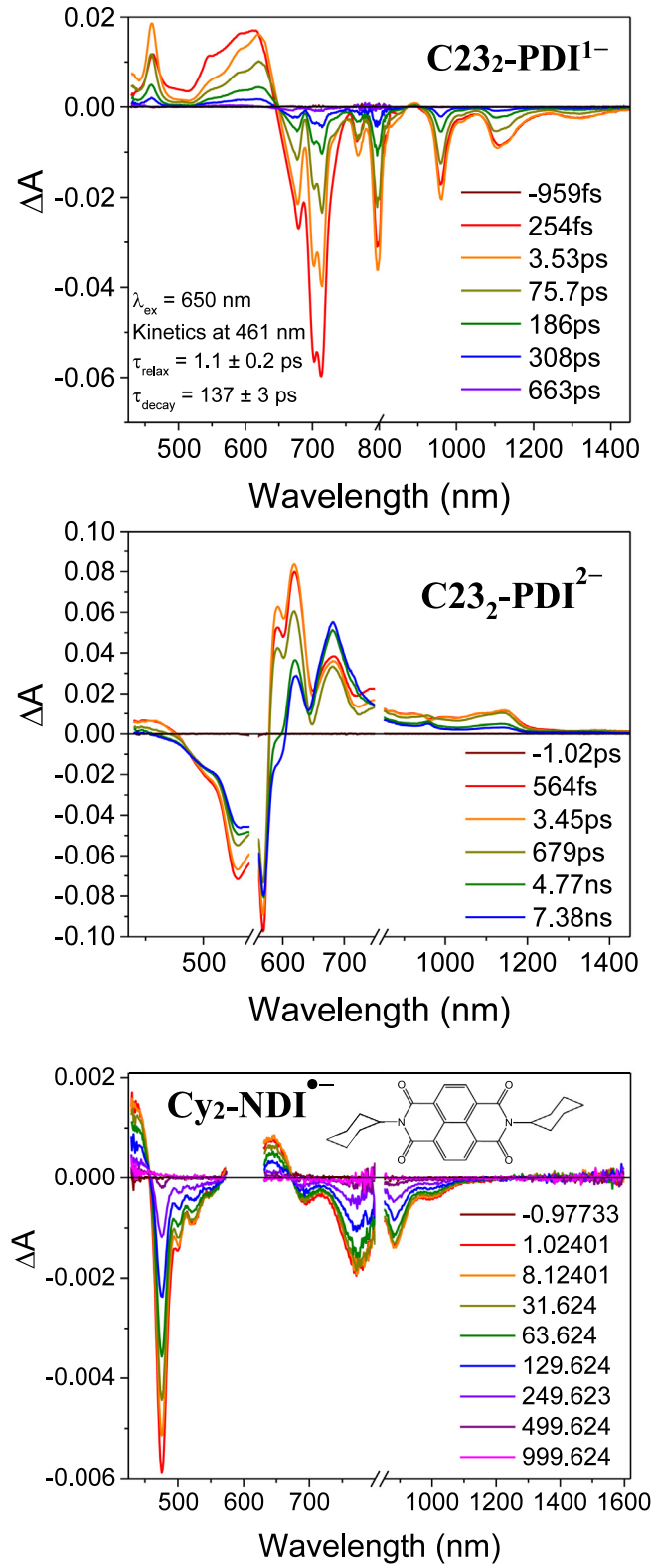

Fig. 4. *Top to bottom*: Visible and NIR transient absorption spectra of **C23$_2$-PDI^{1-}** (λ_{ex} = 650 nm), **C23$_2$-PDI^{2-}** (λ_{ex} = 571 nm) and **Cy$_2$-NDI$^{\cdot-}$** (λ_{ex} = 605 nm). Gaps in the spectra are due to either scattered pump light or gaps in the detector. Originally published in [47] by the Royal Society of Chemistry.

Fig. 6A, and the sum of these contributions is compared to the experimentally observed absorption spectrum in Fig. 6B.

The calculations reveal that three major electronic transitions contribute with appreciable oscillator strength to the visible absorption spectrum, and provide a more elaborate explanation for the electronic absorption spectrum than initially reported by Gosztola et al., [18] where the entire absorption spectrum was presumed to arise from excitation of the unpaired LUMO electron. The D1 transition that dominates the low-energy near-IR absorption of the PDI radical anion arises primarily from excitation of a HOMO electron to pair with the single electron residing in the LUMO, with a 26% component arising from the transition of the unpaired LUMO to the LUMO+1. The D2 transition arises almost exclusively from LUMO → LUMO+2 excitation. These two transitions collectively have much lower oscillator strength than the D3 transition that dominates the blue edge of the absorption around 700 nm. This transition arises primarily from the LUMO → LUMO+1 transition, but does contain 24% HOMO → LUMO character. Multiplying the contributions of each transition by the oscillator strength, we find that approximately 25% of the absorption spectrum involves the filled HOMO orbital. This finding has important implications for the design of substituted PDI molecules intended for use as radical anion chromophores where the effect of the substituents on both the HOMO and LUMO must be considered.

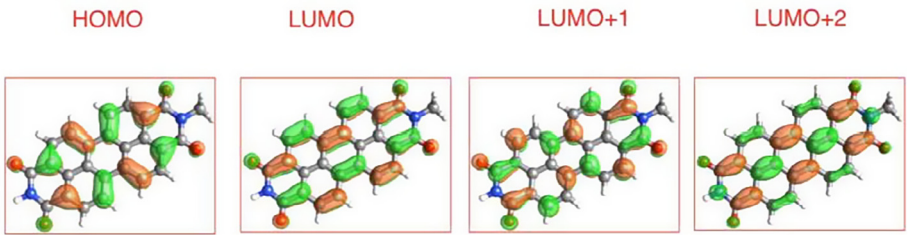

Fig. 5. Frontier molecular orbitals of PDI molecular fragment calculated using DFT (isovalue = 0.03). Originally published in [47] by the Royal Society of Chemistry.

Table 2
The TD-DFT vibronic absorption maximum peak wavelengths $\lambda_{vibronic}$ of the first three electronic transitions, and the vertical wavelengths λ_{vert}, oscillator strengths *f*, and dominant orbital characters for the three lowest-energy calculated electronic transitions of the reduced PDI$^-$ radical. Taken from [47], where the calculated set of the first ten transitions can be found.

State	$\lambda_{vibronic}$ [nm]	λ_{vert} [nm]	*f*	Primary transition character	%	Secondary transition character	%
D1	974.4	844.3	0.032	βHOMO → LUMO	74	αLUMO → LUMO+1	26
D2	688.4	668.6	0.052	αLUMO → LUMO+2	97	N/A	0
D3	710.8	621.4	0.885	αLUMO → LUMO+1	72	βHOMO → LUMO	24

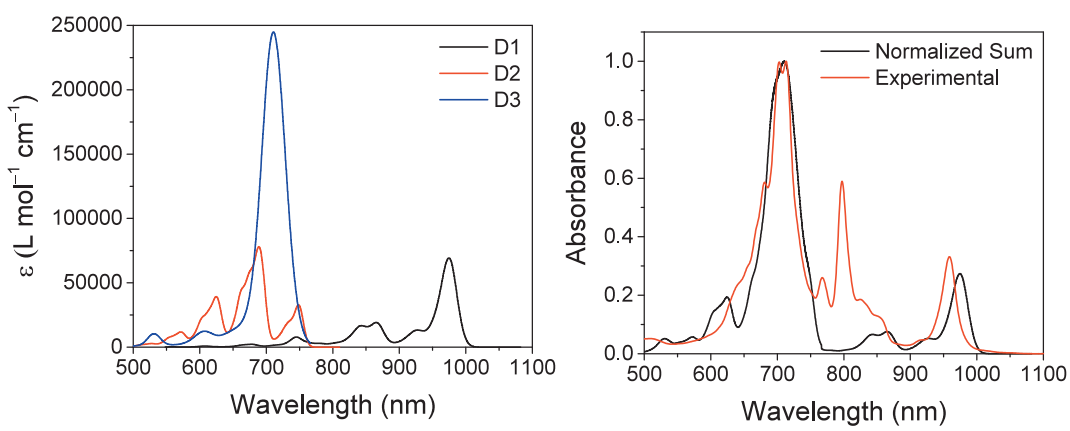

Fig. 6. *Left*: Calculated vibronic transitions from the ground state to the D1 (black), D2 (red) and D3 (blue) states of PDI$^{\cdot-}$. *Right*: Sum of the three calculated vibronic spectra (black) compared to the experimentally determined spectrum of PDI$^{\cdot-}$, normalized to the maximum value. Originally published in [47] by the Royal Society of Chemistry.

4. Systems in which RDI anion is excited

4.1. No intermediate acceptor

4.1.1. Bpy-linked

All the RDI–Re(bpy) complexes in this project were synthesized using a series of cross-coupling reactions to join together the various components. A full discussion of the synthetic scheme for each molecule can be found in the previously published works [47,52,53]. The structure of the bpy-linked dyad molecules that form the prototype for the series is shown in Scheme 2. As will be discussed further below, there is very little coupling between the PDI and the Re(bpy) as shown by electrochemistry, steady-state UV/Vis (Fig. 3, top), and DFT calculation of the frontier orbitals (Fig. 7).

The reduction potentials of the RDI and Re(bpy) moieties of each complex were determined using cyclic voltammetry. The potentials are shown in Table 3 below. Comparison of the reduction potentials of the complexes to those of the **RDI** and **Phbpy-Re-Py** model compounds shows very little effect of complexation on the measured values, indicating minimal coupling between the RDI and Re(bpy) moieties. For spectroscopic measurements, compounds were typically reduced to the RDI radical anion form using TDAE, which undergoes a single reversible two-electron oxidation in DMF at −0.62 V vs SCE [54,55]. To access the PDI dianion, $CoCp_2$ ($E_{½} \sim -0.86$ vs SCE) [56] was employed. While it was possible to access the NDI dianion through the use of $CoCp_2^*$ ($E_{½} \sim -1.44$ vs SCE), this reductant also was capable of reducing the Re(bpy)(CO)$_3$ moiety and accurate, reproducible titration of the sparingly soluble reductant at the very low concentrations (~50–200 μM) of the spectroscopic experiments proved difficult. As a consequence, experiments were performed on the PDI radical anion and dianion, but only on the NDI radical anion.

It was also possible to obtain samples with reduced RDI for spectroscopic experiments by employing *in situ* electrochemical reduction using a home-built spectroelectrochemical cell. Control experiments comparing chemically and electrochemically reduced samples showed no difference in the transient spectroscopy between the two methods. Since chemical reduction was far less time-consuming, that method was employed for all the work discussed in this review.

For each complex in our studies, the Gibbs free energy for each electron transfer step was calculated using the standard equation for Gibbs free energy for the excited-state electron transfer reactions:

$$\Delta G_q = (E_{ox} - E_{red}) - E_{00} + \frac{(Z_{RDI,p}Z_{bpy,p} - Z_{RDI,r}Z_{bpy,r})e^2}{r_{RDI,bpy}\varepsilon_s} + \frac{(Z_{RDI,p}Z_{Re,p} - Z_{RDI,r}Z_{Re,r})e^2}{r_{RDI,Re}\varepsilon_s} + \frac{(Z_{Re,p}Z_{bpy,p} - Z_{Re,r}Z_{bpy,r})e^2}{r_{Re,bpy}\varepsilon_s} \quad (1)$$

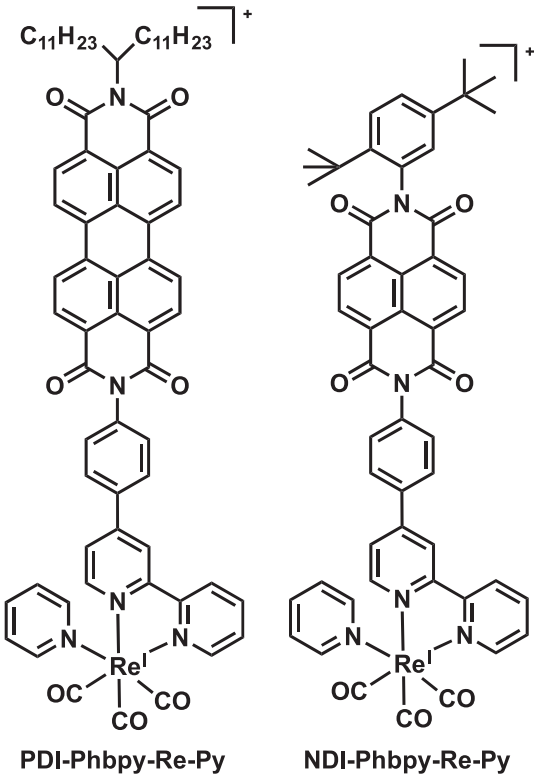

Scheme 2. Structures of the bpy-linked **RDI-Phbpy-Re-Py** compounds.

where E_{ox} and E_{red} are the oxidation and reduction potentials of the donor and acceptor respectively, E_{00} is the energy of the $^{*}RDI^{n-}$ excited state [18], $Z_{RDI,p}$ and $Z_{bpy,p}$, are the charges on the RDI and bpy after electron transfer, $Z_{RDI,r}$, $Z_{bpy,r}$, $Z_{Re,r}$ are the charges on the RDI, bpy, and Re before electron transfer, e is the elementary charge, $r_{RDI,bpy}$, $r_{RDI,Re}$, and $r_{Re,bpy}$ are the donor–acceptor distances (calculated from centroid to centroid using DFT-optimized geometries), and ε_s is the solvent dielectric constant. The inclusion of the charges on each of the RDI, bpy, and Re is necessary because the Re begins in the +1 oxidation state, whereas the RDI begins in a −1 or −2 state, making the reaction a more complex charge shift reaction rather than a simple separation of positive and negative charges.

The Gibbs free energy for the back electron transfer reactions (ΔG_{BET}) can be estimated using the following equation:

$$\Delta G_{ET} = (E_{ox} - E_{red}) + \frac{(Z_{RDI,p}Z_{bpy,p} - Z_{RDI,r}Z_{bpy,r})e^2}{r_{RDI,bpy}\varepsilon_s} + \frac{(Z_{RDI,p}Z_{Re,p} - Z_{RDI,r}Z_{Re,r})e^2}{r_{RDI,Re}\varepsilon_s} + \frac{(Z_{Re,p}Z_{bpy,p} - Z_{Re,r}Z_{bpy,r})e^2}{r_{Re,bpy}\varepsilon_s} \quad (2)$$

which is analogous to the previous equation but without the excited state energy. Donor–acceptor distances are shown in Table 4 below. Calculated ΔG values for each reaction are given in Table 5.

The analysis of the electron transfer behavior of the complexes under study starts by collecting fsTA data. An example of the fsTA results, collected for **PDI^{2-}-Phbpy-Re-Py**, is shown below in Fig. 8A. Because of the extremely fast rate of electron transfer, the excited state of PDI^{2-} decays before the first data point is collected. Observed are the bleaching of the ground-state absorptions of PDI^{2-} from 475–600 nm, and the induced absorptions of $PDI^{\cdot-}$ at wavelengths longer than 600 nm. These features match the ground-state absorptions discussed in Section 3.2. The ground-state bleach and induced absorption features decay back to zero within 250 ps. The kinetic fitting of these features will be discussed further below.

The fsTA data provides information on the dynamics of the chromophore, but to investigate the dynamics of the metal center, fsIR spectroscopy is employed. Femtosecond IR spectra collected on **PDI^{2-}-Phbpy-Re-Py** are shown below in Fig. 9A. The ground-state vibrations of $Re(Phbpy)(CO)_3Py$ at 2046 cm^{-1} and 1928 cm^{-1} are observed to bleach, and induced absorptions characteristic of $Re(Phbpy^{\cdot-})(CO)_3Py$ are observed at 2020 cm^{-1} and 1885 cm^{-1}. The decays of these features can also be fit as described below.

In order to interpret these transient spectroscopic results, we use a global analysis technique. This technique, whose inputs can be generated in one of two ways, has been previously discussed

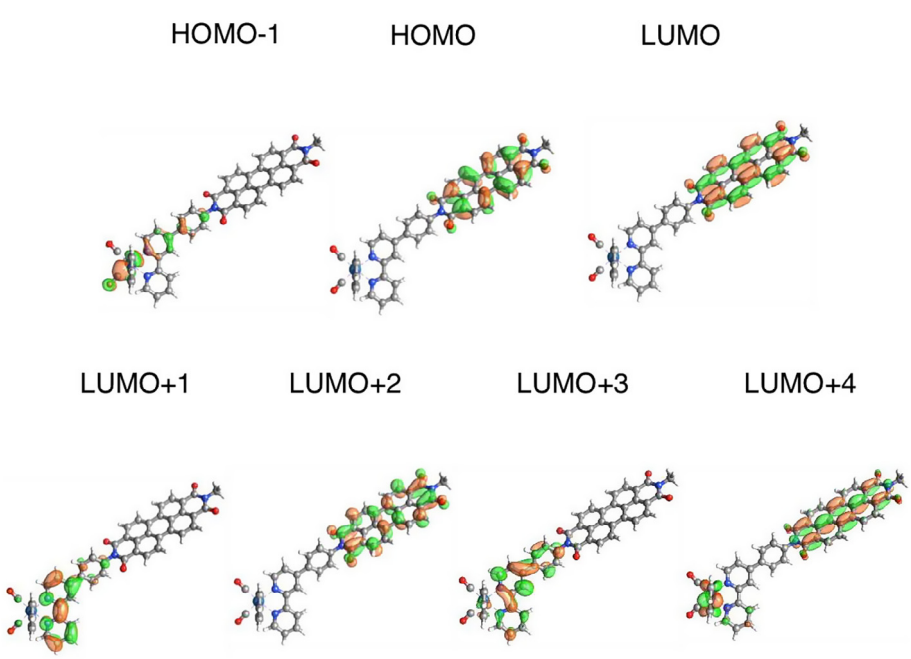

Fig. 7. Calculated frontier molecular orbitals of **PDI-Phbpy-Re-Py**. Originally published in [47] by the Royal Society of Chemistry.

Table 3
Electrochemical redox potentials for the complexes under study, as well as model compounds.[a] Data taken from [47].

	$E_{½}(RDI^{0/-})$ (V)	$E_{½}(RDI^{\cdot-/2-})$ (V)	$E_{½}(bpy^{0/-})$ (V)	$E_{½}(Re^{I/0})$ (V)
PDI[b]	−0.43	−0.70	–	–
NDI[b]	−0.48	−0.99	–	–
Phbpy-Re-Py	–	–	−1.08	−1.53[c]
PDI-Phbpy-Re-Py	−0.51	−0.78	−1.11	−1.45[c]
NDI-Phbpy-Re-Py	−0.50	−1.01	−1.11	−1.47[c]

[a] All electrochemical experiments were performed in DMF with 0.1 M $TBAPF_6$, using a platinum disk working electrode, a platinum wire counter electrode, and a silver wire pseudoreference electrode. Potentials were referenced to a ferrocene internal standard ($E_{½}(Fc^{+/0})$ = 0.45 V) and are given versus the saturated calomel electrode (SCE).
[b] From Ref. [18].
[c] Irreversible, E_{peak} from CV given.

Table 4
Donor–acceptor distances in the complexes under study, calculated from the DFT-optimized geometries. Data taken from [47].

	$r_{RDI,bpy}$ (Å)	$r_{RDI,Re}$ (Å)	$r_{Re,bpy}$ (Å)
PDI-Phbpy-Re-Py	14.2	16.4	2.95
NDI-Phbpy-Re-Py	12.1	14.2	2.95

in detail [47] but a brief description follows. The first input generation technique, singular value decomposition (SVD), factors the two-dimensional data (signal versus time and signal versus frequency) into an orthonormal set of basis spectra that describe the wavelength dependence of the species (the "basis spectra") and the time-dependent amplitude of those basis spectra (the "basis kinetics") [57]. The basis kinetics are then fit using global analysis with shared time/rate constants.

The second technique, multiple-wavelength (MW) fitting, involves simply selecting multiple wavelengths, generally the peaks of the absorptions of the various species thought to be present during the course of the transient experiment. The kinetic traces of each of these wavelengths are globally fit using independent amplitudes and shared time/rate constants. Kinetic traces at various wavelengths for **PDI^{2-}-Phbpy-Re-Py** are shown above in Fig. 9C.

The global analysis method itself involves specifying a kinetic model and using the resulting populations to deconvolute the dataset and reconstruct species-associated spectra. The kinetic model is specified using the rate matrix K, which contains a row and column for each species (A, B, C, etc.) in the fit. The diagonal elements are negative, representing the decay of each species, and the elements in below the diagonal represent the rates with which intermediate species are formed, and the pathways between the species involved. The elements above the diagonal are always zero.

Examples of rate matrices for various kinetic models are shown below. For a simple A → B → (G)round state model, as would be employed for an excited state undergoing electron transfer, followed by back-electron transfer, the matrix is as follows:

$$K = \begin{pmatrix} -k_{A\to B} & 0 \\ k_{A\to B} & -k_{B\to G} \end{pmatrix} \tag{3}$$

where $k_{A\to B}$ is the rate of charge separation and $k_{B\to G}$ is the rate of charge recombination. For a kinetic model A → B → C → (G)round state involving an intermediate electron transfer, the matrix expands thus to include the rate $k_{B\to C}$ representing the rate of the second electron transfer step:

$$K = \begin{pmatrix} -k_{A\to B} & 0 & 0 \\ k_{A\to B} & -k_{B\to C} & 0 \\ 0 & k_{B\to C} & -k_{C\to G} \end{pmatrix} \tag{4}$$

More complicated kinetic models, in which one species decays into a combination of two species that each decay independently to ground, can be written by filling in more of the below-diagonal elements, as in the case of the model A → B + C → (G) round state:

$$K = \begin{pmatrix} -(k_{A\to B} + k_{A\to C}) & 0 & 0 \\ k_{A\to B} & -k_{B\to G} & 0 \\ k_{A\to C} & 0 & -k_{C\to G} \end{pmatrix} \tag{5}$$

in which species A decays to a combination of species B and species C with the combined rate $k_{A\to B}$ + $k_{A\to C}$, species B decays to ground with the rate $k_{B\to G}$, and species C decays to ground state with the rate $k_{C\to G}$.

Any arbitrary decay model can be written as a rate matrix in this way. The differential equations specified by the rate matrix are then solved using matrix methods and the solutions are convoluted with a Gaussian instrument response function with a specified width (generally 0.3 ps for femtosecond experiments, and 0.6 ns for nanosecond experiments). These solutions are then fit using least-squares fitting to obtain a best fit to either the basis kinetics (in the case of SVD) or to the kinetic traces at each wavelength, as shown in Fig. 8C below.

Once the rates have been determined, they are fed back into the differential equations and solved for the populations of each state, producing equations A(t), B(t), C(t), and so on. The equations determined for **PDI^{2-}-Phbpy-Re-Py** are plotted in Fig. 8D. The full set of two-dimensional data is then deconvoluted with the populations as functions of time to produce reconstructed spectra for each species (the "species-associated spectra"), shown in Fig. 8B.

In the case of **NDI$^{\cdot-}$-bpy-Re-py** and **PDI^{2-}-bpy-Re-py**, the data fit well to an A → B → (G)round state model, implying that the excited state undergoes electron transfer to produce the oxidized RDI chromophore and the reduced bpy ligand, followed by back-electron transfer. This model is represented graphically as a Jablonski diagram in Fig. 10. The production of the oxidized RDI

Table 5
Rates and Gibbs free energy of electron transfer reactions discussed in this section. Data taken from [47].

	RDI^{n-}	τ_{ex} (ps)	τ_{ET} (ps)	ΔG_q (eV)	τ_{BET}	ΔG_{BET} (eV)
PDI-bpy-Re-Py	1−	53.5 ± 1.4	23.4	−0.81	53.5 ± 1.4 ps	−0.49
	2−	<0.3	<0.3	−1.47	107 ± 1 ps	−0.25
NDI-bpy-Re-Py	1−	0.4 ± 0.1	0.4	−1.10	31.8 ± 0.8 ps	−0.50

τ_{ex}: Observed excited state lifetime; τ_{ET}: Calculated excited state electron transfer rate; k_{ET}: Calculated excited state electron transfer rate; ΔG_q: Driving force for $^{*}RDI^{n-}$ → bpy electron transfer; τ_{BET}: Back electron transfer lifetime; k_{BET}: Back electron transfer rate; ΔG_{BET}: Gibbs free energy for $bpy^{\cdot-}$ → $RDI^{(n-1)-}$ back electron transfer.

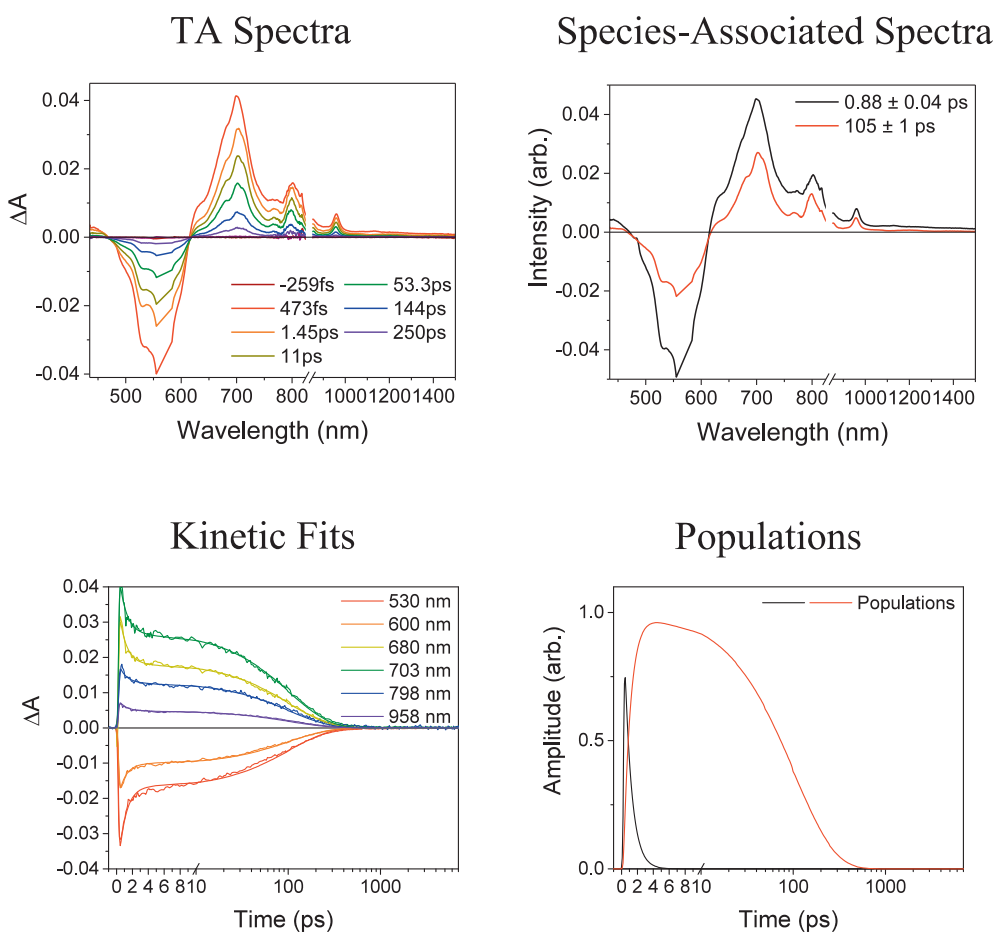

Fig. 8. Transient absorption spectra, species-associated spectra, global multiple-wavelength kinetic traces and fits, and populations of each species for **PDI^{2-}-Phbpy-Re-Py** (λ_{ex} = 570 nm). Originally published in [47] by the Royal Society of Chemistry.

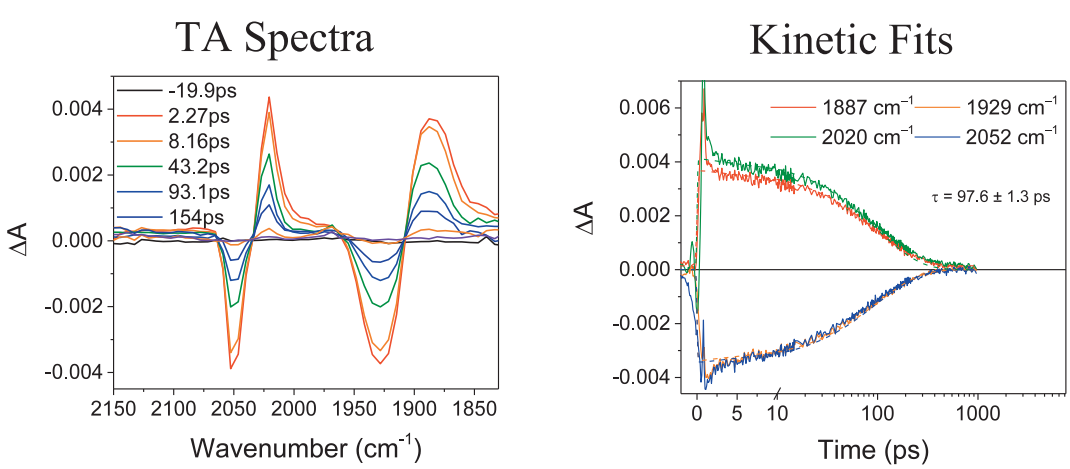

Fig. 9. Time-resolved IR spectra and global multiple-wavelength kinetic traces and fits for **PDI^{2-}-Phbpy-Re-Py** (λ_{ex} = 570 nm). Originally published in [47] by the Royal Society of Chemistry.

chromophore is supported by the visible/NIR TA data showing the formation of induced absorptions corresponding to either neutral NDI or PDI radical anion, as appropriate. The production of the reduced bpy ligand is supported by the fsIR data, which show the formation of induced absorptions at lower energies than the ground-state bleaches. These induced absorptions correspond to the CO stretches of the bpy-centered radical anion of Re(Phbpy)$(CO)_3$Py shown in Fig. 3 above (Section 3.2). The rates determined using fsTA and fsIR data match one another within the error of the fitting procedure, lending support to the proposed mechanism. The rates determined for each electron transfer step are given in Table 5.

In the complex **PDI$^{\cdot-}$-Phbpy-Re-Py** the electron transfer kinetics are more complicated, and are different depending on

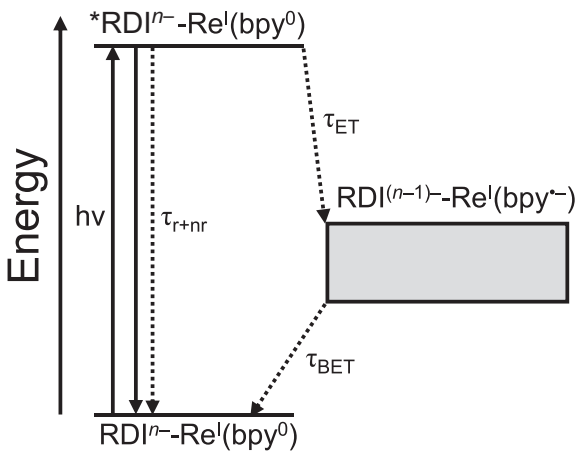

Fig. 10. Energy level diagram showing general scheme of electron transfer in **RDI^{n-}-Phbpy-Re-Py** complexes after excitation. Energy of the charge-transfer state is shown as a range to reflect the different energies of different complexes. Originally published in [47] by the Royal Society of Chemistry.

the excitation wavelength (680 nm vs 950 nm). When the complex is excited at 950 nm, shown in Fig. 11A, the ground-state absorptions of PDI^{1-} bleach immediately, and induced absorptions and stimulated emission features characteristic of *PDI^{1-} form. These features are identical to those described in Section 3.3. As the spectrum evolves, the excited-state features lessen in intensity but do not decay completely, while features characteristic of neutral PDI appear. Global fitting using SVD of these data to an A → B → ground state model show that the first species-associated spectrum (Fig. 11B, black), with a time constant of 24 ps, consists solely of *PDI$^{\bullet-}$ features, while the second species-associated spectrum, with a time constant of 52 ps (Fig. 11B, red), contains both *PDI$^{\bullet-}$ and PDI^{0} features. This result indicates that the two species are decaying concurrently, which points to an equilibrium existing between the two states. The existence of this equilibrium is supported by temperature-dependent fsTA data, shown in Fig. 12, showing a relationship between temperature and the ratio of the intensity of *PDI$^{\bullet-}$ features and PDI^{0} features (and by extension, the ratio of the concentration of those two species).

When the complex is excited at 680 nm, however, the fsTA data at short times (Fig. 11C) look quite different. Instead of growing in with a time constant of 24 ps, PDI^{0} features are already visible within the instrument response. Global analysis still allows the data to be fit to two species in an A → B → ground model, however the first basis spectrum now corresponds to a species with a lifetime of only 2 ps. That species (Fig. 11D, black) has features of both *PDI$^{\bullet-}$ and PDI^{0}, and decays to a second species (Fig. 11D, red) whose basis spectrum and lifetime are very similar to the second species obtained upon excitation at 950 nm (Fig. 11B, red).

TD-DFT calculations indicate that the PDI–Re(bpy) complex has a CT excited state that is calculated to be isoenergetic (within the ~0.2 eV error of the TD-DFT calculations) with the lowest PDI-localized state (D1). This transition corresponds to excitation of the unpaired electron in the PDI$^{\bullet-}$ LUMO into the empty bpy LUMO. The transition to this state, denoted *[PDI^{0}-Re(bpy$^{\bullet-}$)], has negligible oscillator strength due to the weak electronic coupling and poor orbital overlap between the PDI and Re(bpy) moieties. However, it can be populated by thermal electron transfer or internal

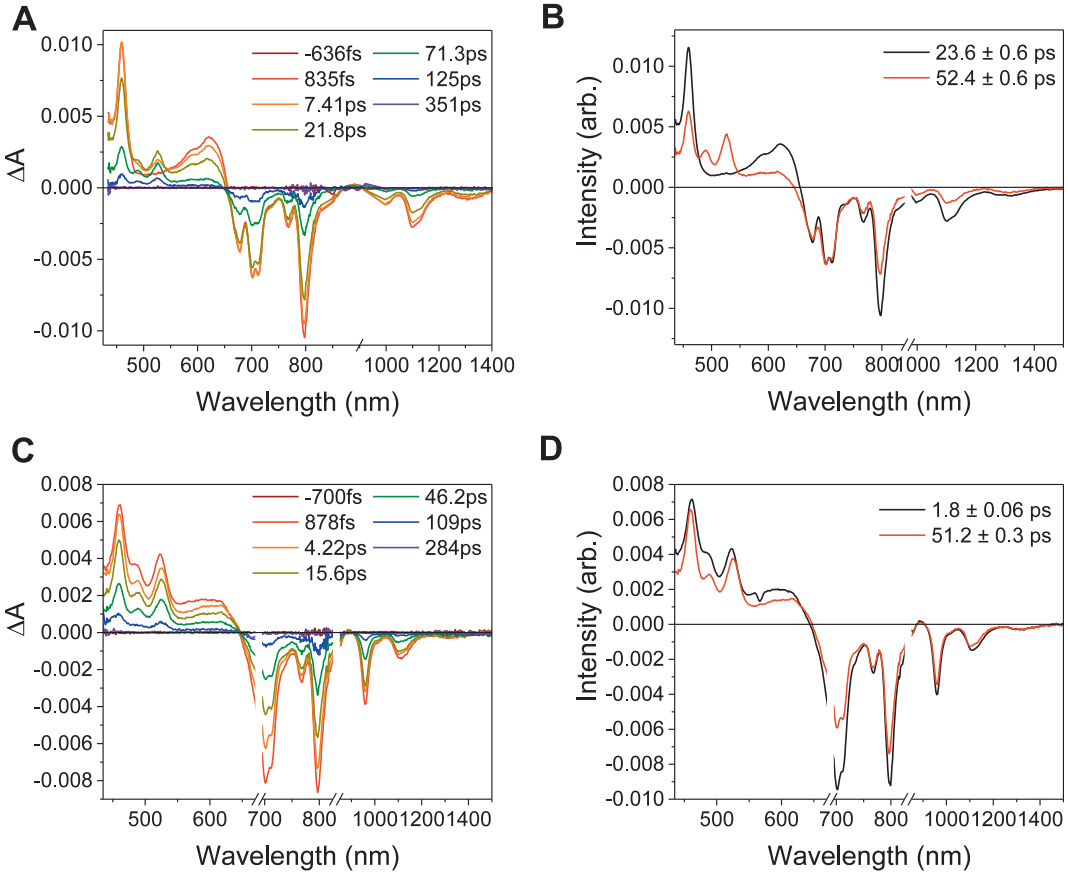

Fig. 11. (A) Transient absorption spectra and (B) species-associated spectra for **PDI$^{\bullet-}$-Phbpy-Re-Py** (λ_{ex} = 950 nm). (C) Transient absorption spectra and (D) species-associated spectra of those spectra for **PDI$^{\bullet-}$-Phbpy-Re-Py** (λ_{ex} = 680 nm). Originally published in [47] by the Royal Society of Chemistry.

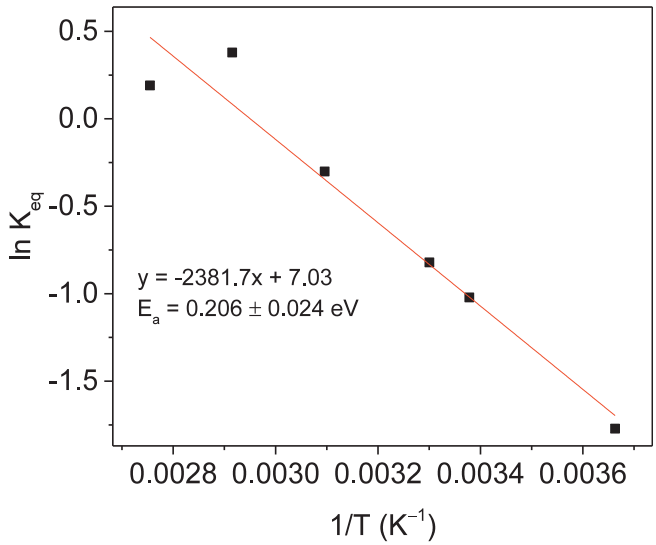

Fig. 12. Plot of ln K_{eq} vs. $1/T$ derived from the [PDI^0]:[*PDI^1$^-$] ratio in the SVD spectra of variable-temperature TA experiments on **PDI$^{\bullet-}$-Phbpy-Re-Py**. Originally published in [47] by the Royal Society of Chemistry.

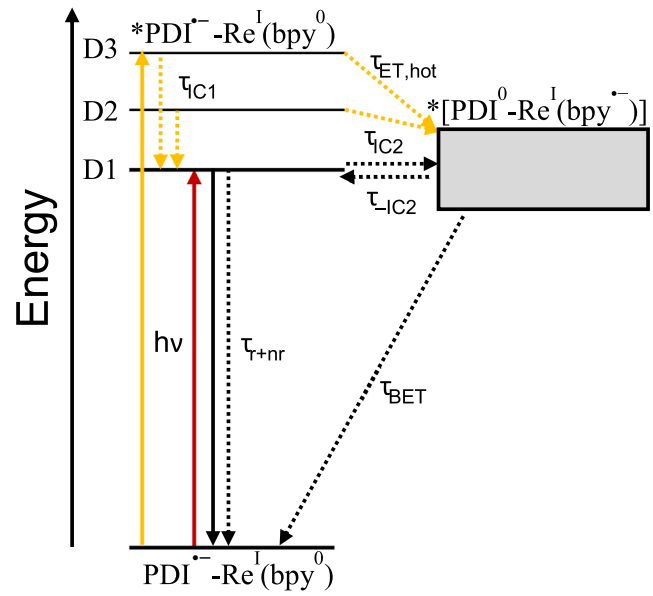

Fig. 13. Jablonski diagram showing electron transfer in **PDI$^{\bullet-}$-Phbpy-Re-Py** after excitation at 950 nm (red) or 680 nm (yellow). Energy of the charge-transfer state is shown as a range to reflect the uncertainty of the exact energy of this state. Originally published in [47] by the Royal Society of Chemistry.

conversion from *PDI$^{\bullet-}$, with which it is in thermal equilibrium. It is that equilibrium that gives rise to the concomitant decay of the *PDI$^{\bullet-}$ and PDI^0 features observed at both excitation wavelengths.

The change in dynamics as the excitation wavelength is varied is due to the electronic excited-state manifold of PDI$^{\bullet-}$ described in Section 3.3. Excitation at 680 nm produces the ^{*D3}PDI$^{\bullet-}$ excited state, which decays via a combination of internal conversion (τ_{IC1}) and electron transfer ($\tau_{ET,\ hot}$) to the equilibrium ^{*D1}PDI$^{\bullet-}$ $\rightleftharpoons$ *[PDI^0-Re(bpy$^{\bullet-}$)]. This decay occurs within the instrument response. Excitation at 950 nm only produces ^{*D1}PDI$^{\bullet-}$, which undergoes slower electron transfer/internal conversion (τ_{IC2}) to establish the ^{*D1}PDI$^{\bullet-}$ $\rightleftharpoons$ *[PDI^0-Re(bpy$^{\bullet-}$)] equilibrium. This equilibrium then decays via a combination of radiative and nonradiative decay of the D1 state (τ_{r+nr}) and back-electron transfer of the *[PDI^0-Re(bpy$^{\bullet-}$)] state (τ_{BET}). A summary of these decay pathways is shown as a Jablonski diagram in Fig. 13.

An interesting implication of the observation that different excitation wavelengths lead to different kinetics in the **PDI$^{\bullet-}$-Phbpy-Re-Py** concerns the results reported by Majima and co-workers on their dyads of PDI with various acceptors [35]. In their work, Majima and co-workers report exciting the PDI radical anion at 700 nm, presumably due to the limitations of their experimental setup. As demonstrated above, multiple electronic transitions contribute to the visible/NIR absorption spectrum of PDI$^{\bullet-}$ at that wavelength [47] and contrary to the results shown by Gosztola et al. in 2000 [18], which were relied upon by Majima and co-workers to validate their decision to excite PDI$^{\bullet-}$ at 700 nm, we have observed that electron transfer from a higher excited state is possible before that state relaxes to the D1 state. Because Majima and co-workers calculate the driving force for electron transfer based on the energy of the D1 state, and subsequently use the combination of calculated driving force and observed electron transfer rate to fit a Marcus theory expression to derive the reorganization energy, it is possible that the rates they observe are not correctly correlated to the driving forces calculated. In light of our observations it will be necessary to re-examine those results before the calculated reorganization energies can be relied upon.

4.1.2. Intermediate acceptor

In an effort to increase the lifetime of the charge-separated state in the bpy-linked dyads discussed in Section 4.1.1, we investigated the possibility of introducing an intermediate electron acceptor between the NDI$^{\bullet-}$ and the Re(bpy)(CO)$_3$L moieties [53]. The function of the intermediate acceptor is to maintain the rapid oxidative quenching of the NDI$^{\bullet-}$ excited state, but to then allow the electron to move further away from the NDI^0 and lower the coupling between NDI and Re(bpy)(CO)$_3$L, so as to lengthen the lifetime of the charge-separated state. After careful consideration, diphenylanthracene (DPA) was chosen as the intermediate acceptor, and the ligand **NDI-DPA-bpy** and the triad **NDI-DPA-Re(bpy)** were synthesized (Scheme 3). The reduction potential of DPA is positioned in between the excited-state oxidation potential of *NDI$^{\bullet-}$ (−2.16 V vs SCE) and the reduction potential of the bpy ligand in Re(bpy)(CO)$_3$L (redox potentials determined by cyclic voltammetry are shown in Table 6). Comparison of the NDI and Re(bpy) redox potentials to those of model compounds (see Section 4.1.1) indicates minimal coupling between the various fragments of the molecule. Using the redox potentials and DFT-calculated donor–acceptor distances for each moiety, ΔG values for each electron transfer step are shown in Table 7.

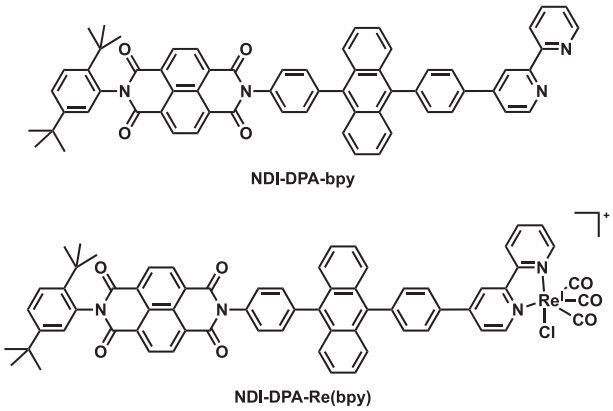

Scheme 3. The ligand **NDI-DPA-bpy** and the triad **NDI-DPA-Re(bpy)**.

Table 6
Redox potentials (vs. SCE using a Fc/Fc^+ reference at 0.45 V vs SCE). Data taken from [53].

	$NDI^{0/-}$	$NDI^{-/2-}$	$bpy^{0/-}$	$Re^{I/0}$	$DPA^{0/-}$
NDI-DPA-bpy	−0.51	−1.03	–	–	−1.90
NDI-DPA-Re(bpy)	−0.51	−1.03	−1.26	−1.72	−1.90

Table 7
Driving force for electron transfer reactions in **NDI-DPA-Re(bpy)**. Data taken from [53].

Process	ΔG (eV)
$^*NDI^{\cdot-} \rightarrow DPA$	−0.24
$DPA^{\cdot-} \rightarrow Re(bpy)$	−0.64
$DPA^{\cdot-} \rightarrow NDI^0$	−1.37
$Re(bpy^{\cdot-}) \rightarrow NDI^0$	−0.73

In the unreduced state, **NDI-DPA-Re(bpy)** displays steady-state absorptions characteristic of both NDI and DPA in the near-UV (Fig. 14). Those absorptions are underlain by the broad Re → bpy MLCT band. When the complex is reduced, the NDI^0 absorptions disappear and are replaced by the characteristic $NDI^{\cdot-}$ absorptions in the visible and near-IR (see Section 3.2), while the DPA absorptions in the near-UV remain, along with the Re → bpy MLCT band.

The fsTA and fsIR spectra collected for **$NDI^{\cdot-}$-DPA-Re(bpy)** are shown in Figs. 15 and 16. As expected, at short times after excitation the ground state features of $NDI^{\cdot-}$ bleach, and features attributable to $^*NDI^{\cdot-}$ appear at 425 nm and 600–750 nm. The excited-state features decay with a lifetime of 14.5 ps (species-associated spectra and SVD kinetics shown in Fig. 15B and C), while a peak characteristic of NDI^0 appears at 380 nm. On the same timescale, the CO stretches of $Re(Phbpy)(CO)_3Cl$ are observed to bleach in the fsIR, and features characteristic of $Re(Phbpy^{\cdot-})(CO)_3Cl$ appear. No features attributable to $DPA^{\cdot-}$ (absorptions from 600–900 nm) are detected, indicating that electron transfer from $^*NDI^{\cdot-}$ to DPA is slower than electron transfer from DPA to $Re(Phbpy)(CO)_3Cl$, preventing buildup of the $DPA^{\cdot-}$ species. Experiments on the **$NDI^{\cdot-}$-DPA-bpy** ligand indicate that back-electron transfer from $DPA^{\cdot-}$ to NDI^0 occurs with a lifetime of 5 ps, meaning that the forward electron transfer from $DPA^{\cdot-}$ to $Re(Phbpy)(CO)_3Cl$ must occur with a lifetime substantially faster than that. After the $DPA^{\cdot-}$ to $Re(Phbpy)(CO)_3Cl$ electron transfer, the NDI^0 features in the nsTA and the $Re(Phbpy^{\cdot-})(CO)_3Cl$ features in the fsIR decay with a lifetime of 24.5 ns. This lifetime is about 800 times longer than the lifetime of the charge-separated state in **$NDI^{\cdot-}$-Phbpy-Re-Py**, which has a lifetime of only 31.8 ps. The energy levels and rates for this triad

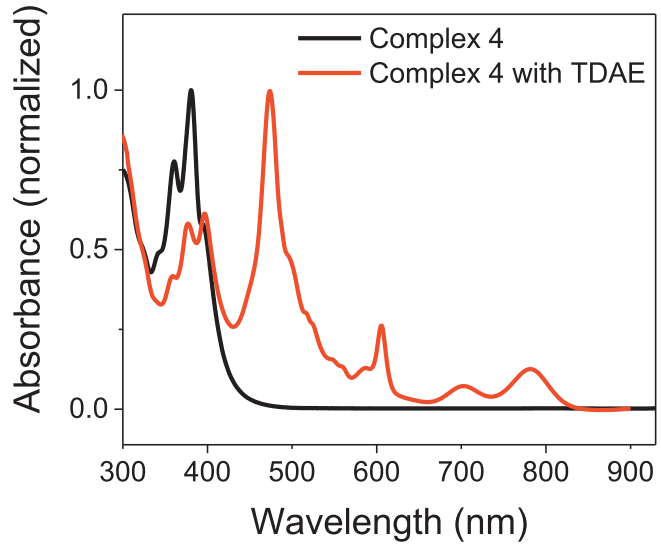

Fig. 14. Electronic absorption spectra of **NDI-DPA-Re(bpy)** in DMF with and without the TDAE reductant added. Reproduced with permission from [53].

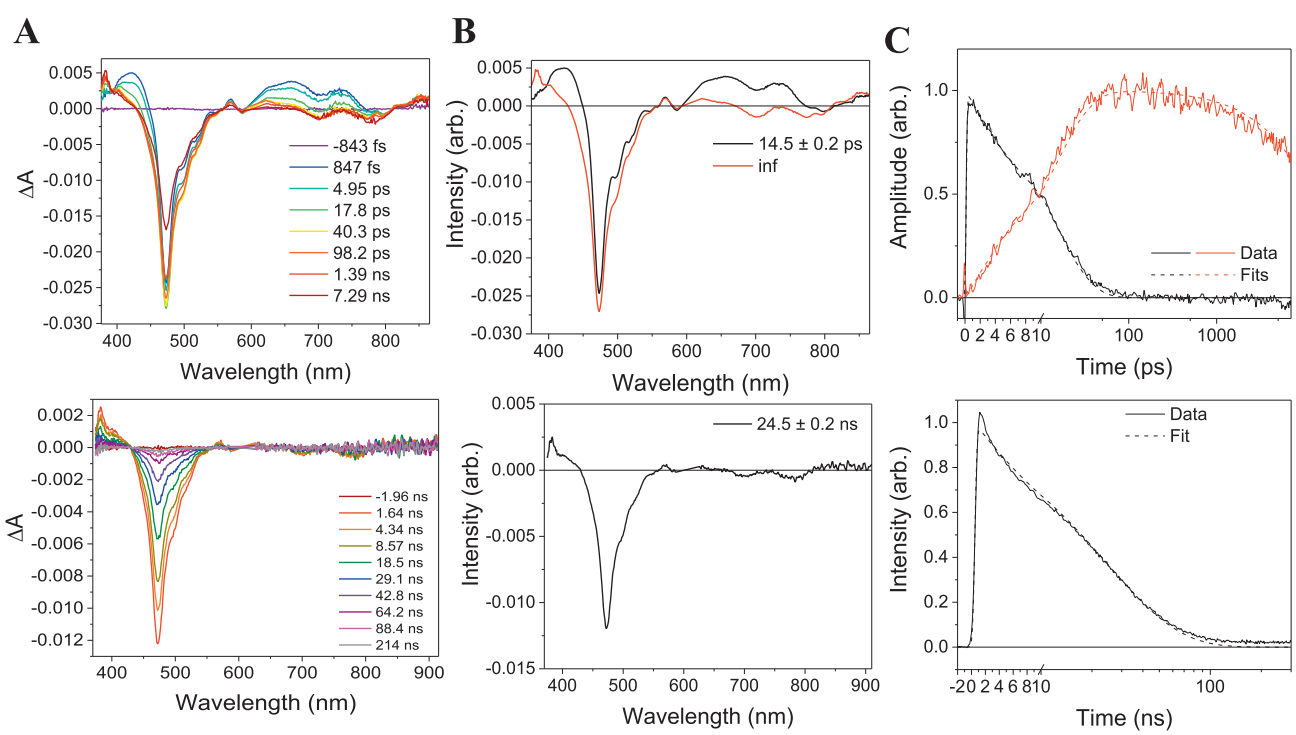

Fig. 15. Transient absorption data for **$NDI^{\cdot-}$-DPA-Re(bpy)** in DMF (λ = 605 nm). (A) Transient absorption spectra; (B) species-associated spectra; (C) singular value decomposition kinetic traces and fits. Reproduced with permission from [53].

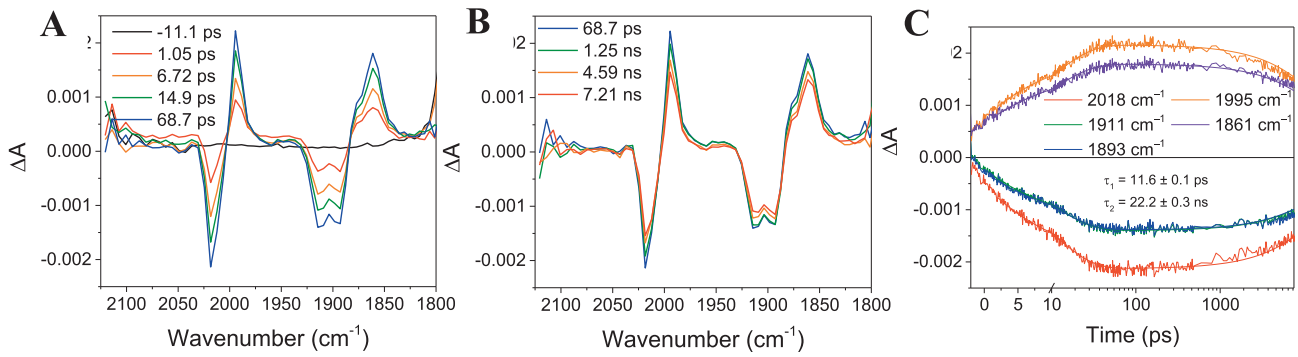

Fig. 16. (A and B) Time-resolved IR spectra and (C) global multiple-wavelength kinetic traces and fits for **NDI$^{\bullet-}$-DPA-Re(bpy)** in DMF (λ = 605 nm). Reproduced with permission from [53].

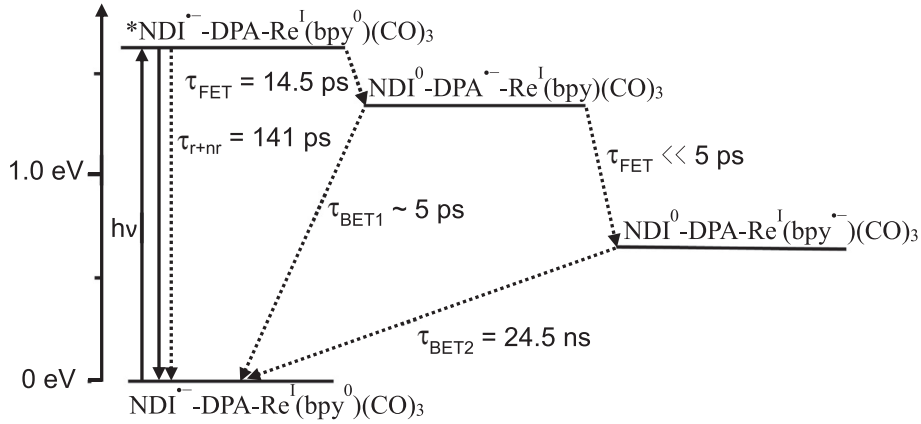

Fig. 17. Energy-level diagram for **NDI$^{\bullet-}$-DPA-Re(bpy)**. Energies are obtained from Table 7. Reproduced with permission from [53].

system are summarized graphically in a Jablonski diagram shown in Fig. 17.

4.2. Py-linked

4.2.1. No intermediate acceptor

As part of the initial study into RDI–Re(bpy) complexes, compounds **Phbpy-Re-PyPhNDI** and **Phbpy-Re-PyPhPDI** were synthesized in which the RDI chromophore is linked to the Re(bpy) center through a pyridine ligand (Scheme 4) [47]. While these complexes are not suitable for catalytic reduction of CO_2 due to the dissociation of the pyridine ligand as part of the catalytic cycle [27,28] it is interesting to compare their photophysical properties with those of the bpy-linked complexes discussed above in Section 4.1.1.

The electrochemistry of the **Phbpy-Re-PyPhRDI** complexes is practically identical to that of the bpy-linked complexes discussed in Section 4.1.1. The reduction potentials are shown in Table 8. Comparison with the isolated fragments (Table 3 in Section 4.1.1) shows that there is minimal coupling between the RDI and Re(bpy)$(CO)_3$ moieties.

Just like the **RDI-Phbpy-Re-Py** complexes, the ground-state spectra of the **Phbpy-Re-PyPhRDI** complexes exhibit the ground-state features of the two components. As an example, the spectrum of **Phbpy-Re-PyPhNDI** is shown in Fig. 3, bottom. In the neutral form, the NDI^0 and Re(bpy)$(CO)_3$Py absorptions overlap in the near-UV and tail into the visible. When the NDI is reduced, the

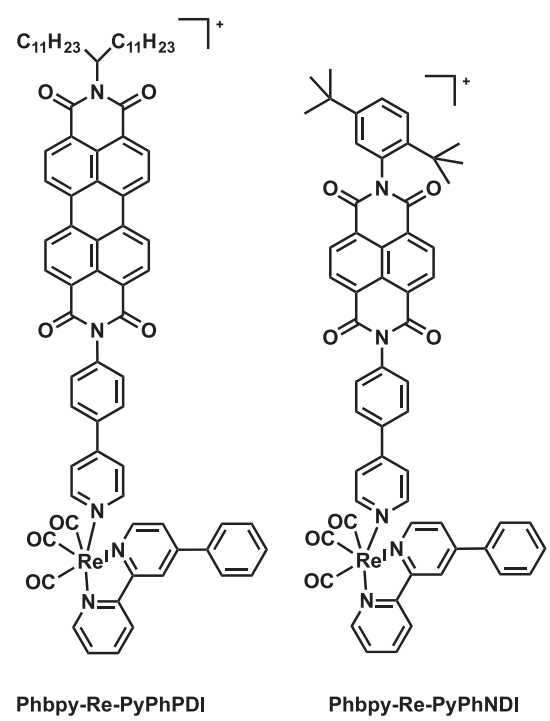

Scheme 4. Structures of the **Phbpy-Re-PyPhRDI** compounds.

Table 8
Electrochemical redox potentials for the complexes in this section.[a] Data taken from [47].

	$E_{½}$(RDI$^{0/-}$) (V)	$E_{½}$(RDI$^{-/2-}$) (V)	$E_{½}$(bpy$^{0/-}$) (V)	$E_{½}$(Re$^{I/0}$) (V)
Phbpy-Re-PyPhPDI	−0.47	−0.74	−1.06	−1.47[b]
Phbpy-Re-PyPhNDI	−0.50	−1.05	−1.10	−1.47[b]

[a] All electrochemical experiments were performed in DMF with 0.1 M $TBAPF_6$, using a platinum disk working electrode, a platinum wire counter electrode, and a silver wire pseudoreference electrode. Potentials were referenced to a ferrocene internal standard ($E_{½}$(Fc$^{+/0}$) = 0.45 V) and are given versus the saturated calomel electrode (SCE).
[b] Irreversible, E_{peak} from CV given.

Re → bpy MLCT absorption remains, while the NDI$^{\cdot-}$ absorptions appear in the visible and NIR. There is no evidence for a CT band in the visible region.

Qualitatively, the TA spectra for the **Phbpy-Re-PyPhRDI^{n-}** compounds look similar to those obtained for the **RDI^{n-}-Phbpy-Re-Py** compounds, only with slower rates for both forward and back-electron transfer. Shown in Fig. 18 is an example, taken on **Phbpy-Re-PyPhPDI$^{\cdot-}$** with 950 nm excitation. At short times after excitation, the ground-state absorptions of PDI$^{\cdot-}$ from 650 to 950 nm are observed to bleach, and induced absorptions and stimulated emission bands at 450–650 nm and 960–1300 nm, respectively, are observed. The induced absorption and stimulated emission features decay as bands characteristic of PDI^0 at 485 nm and 525 nm appear. These features slowly decay, not returning to the ground state by the end of the fsTA experiment (8 ns). The fsTA data can be fit to an A → B → ground state model with lifetimes of A and B being 105 ps and 17.1 ns, respectively. Due to experimental limitations, it was not possible to collect fsIR data with a 950 nm pump, but fsIR data collected with a 705 nm pump show bleaching of the ground state CO stretches and induced absorption of the Re(bpy$^{\cdot-}$)(CO)$_3$ CO stretches as predicted (Fig. 19). Due to the different pump wavelength (see Section 4.1.1) the kinetics do not match those observed in the fsTA experiment with a longer-wavelength pump, but the fact that the spectral features match those predicted for a complex with a reduced bpy ligand confirms that the electron transfer is taking place. Similar data were obtained for **Phbpy-Re-PyPhPDI^{2-}** and **Phbpy-Re-PyPhNDI$^{\cdot-}$** and the rates obtained from those experiments are shown in Table 9.

The large difference in electron-transfer rates between the **Phbpy-Re-PyPhRDI^{n-}** and the **RDI^{n-}-Phbpy-Re-Py** complexes can

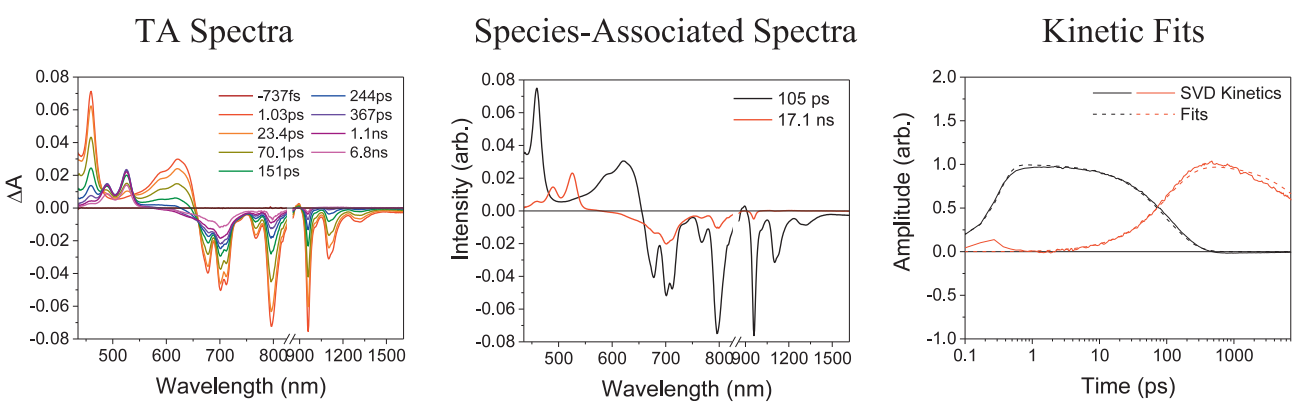

Fig. 18. Transient absorption spectra, species-associated spectra, and singular value decomposition kinetic traces and fits for **Phbpy-Re-PyPhPDI$^{\cdot-}$** (λ_{ex} = 950 nm). Originally published in [47] by the Royal Society of Chemistry.

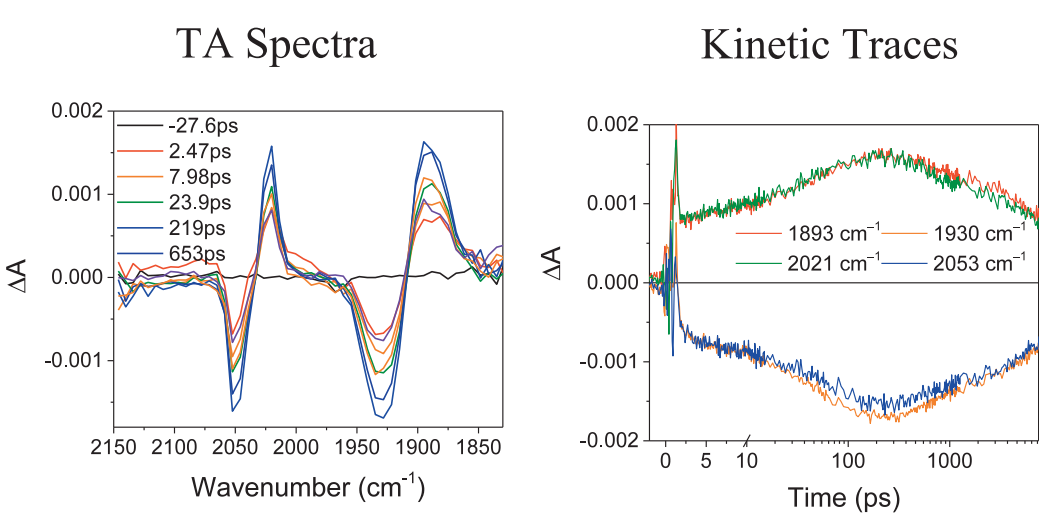

Fig. 19. Time-resolved IR spectra and global multiple-wavelength kinetic traces and fits for **Phbpy-Re-PyPhPDI$^{\cdot-}$** (λ_{ex} = 705 nm). Originally published in [47] by the Royal Society of Chemistry.

Table 9
Rates and Gibbs free energies of electron transfer reactions discussed in this section. Data taken from [47].

	RDI^{n-}	τ_{ex} (ps)	τ_{ET} (ps)	ΔG (eV)	τ_{BET}	ΔG_{BET} (eV)
Phbpy-Re-PyPhPDI	1−	105 ± 0.9	381	−0.82	17.1 ± 0.2 ns	−0.48
	2−	0.9 ± 0.2	0.9	−1.49	268 ± 1 ns	−0.23
Phbpy-Re-PyPhNDI	1−	1.5 ± 0.1	1.5	−1.11	29.7 ± 0.2 ns	−0.49

τ_{ex}: Observed excited state lifetime; τ_{ET}: Calculated excited state electron transfer rate; k_{ET}: Calculated excited state electron transfer rate; ΔG_q: Driving force for $^*RDI^{n-} \rightarrow$ bpy electron transfer; τ_{BET}: Back electron transfer lifetime; k_{BET}: Back electron transfer rate; ΔG_{BET}: Gibbs free energy for $bpy^- \rightarrow RDI^{(n-1)-}$ back electron transfer

Table 10
Donor–acceptor distances in the complexes in this section, calculated from the DFT-optimized geometries. Data taken from [47].

	$r_{RDI,bpy}$ (Å)	$r_{RDI,Re}$ (Å)	$r_{Re,bpy}$ (Å)
Phbpy-Re-PyPhPDI	16.9	16.4	2.83
Phbpy-Re-PyPhNDI	14.5	14.3	2.95

be rationalized on the basis of distance and geometry. The RDI donor and bpy acceptor moieties in **RDI-Phbpy-Re-Py** are 14.2 Å and 12.1 Å for the PDI and NDI complexes, respectively. In the **Phbpy-Re-PyPhRDI** complexes these distances are 16.9 Å and 14.5 Å for the PDI and NDI complexes, respectively (see Table 10). In addition, in the **RDI-Phbpy-Re-Py** complexes, the two moieties are separated only by a phenyl group, and the RDI is able to rotate to be in plane with the bpy, increasing the coupling. In the **Phbpy-Re-PyPhRDI** complexes, the two moieties are separated by the Re center and the octahedral ligand environment prevents the RDI from rotating to be in plane with the bpy ligand, decreasing the coupling. As a result, the forward electron transfer rates are 3–5 times faster in the bpy-linked than in the Py-linked complexes, and the back-electron transfer rates are 500–1000 times faster in the bpy-linked complexes. While the Py-linked Re(bpy) complexes are not useful for catalytic studies because of the nature of the catalytic cycle, this finding does suggest that in complexes where the pyridine ligand does not dissociate, it would be possible to use a pyridine-linked chromophore and obtain a long charge-separated lifetime.

4.2.2. Using an intermediate acceptor

Just as in Section 4.1.2 above, the lifetime of the charge-separated state in the pyridine-bound chromophore complexes can be lengthened by the introduction of a DPA intermediate electron acceptor [52]. The structures of the ligand **NDI-DPA-PhPy** and the Re complex **NDI-DPA-PhPy-Re(dmb)** are shown in Scheme 5. As with the **NDI-DPA-Re(bpy)Cl** complex discussed in Section 4.1.2, there is minimal coupling among the three components of the system, as shown by electrochemistry (Table 11) and steady-state spectroscopy (Fig. 20). Donor–acceptor distances

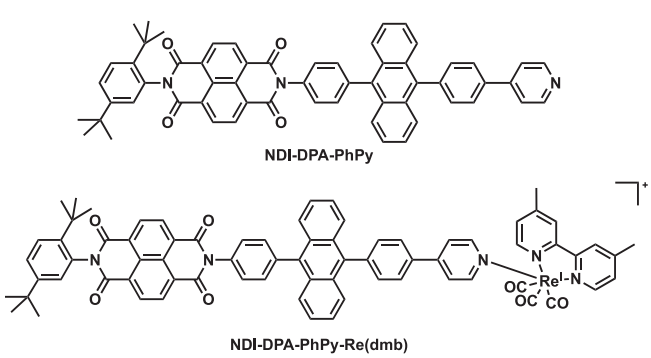

Scheme 5. Structure of the **NDI-DPA-PhPy** ligand and **NDI-DPA-PhPyRe(dmb)** triad.

Table 11
Redox potentials (vs. SCE using a Fc/Fc^+ reference at 0.45 V vs SCE). Data taken from [52].

	$NDI^{0/-}$	$NDI^{-/2-}$	$dmb^{0/-}$	$Re^{I/0}$	$DPA^{0/-}$
NDI-DPA-PhPy	−0.51	−1.02	–	–	−1.86
NDI-DPA-PhPyRe(dmb)	−0.51	−1.02	−1.16	−1.56	−1.86

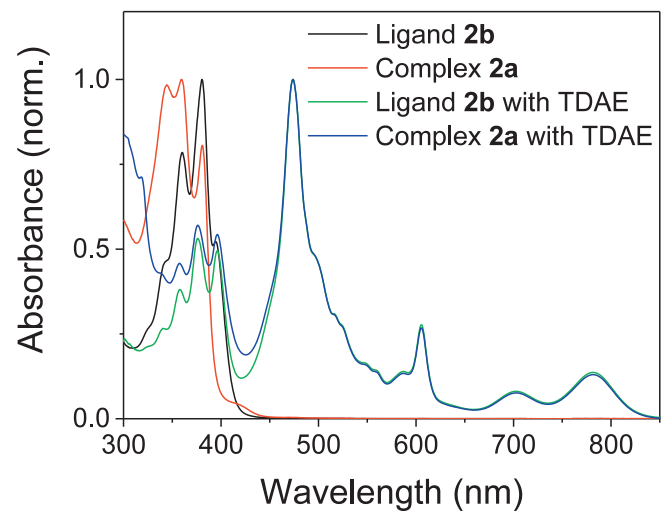

Fig. 20. Electronic absorption spectra of **NDI-DPA-PhPy** and **NDI-DPA-PhPy-Re (dmb)** in DMF with and without the TDAE reductant added. Reproduced from [52] with permission from the Royal Society of Chemistry.

calculated from DFT-optimized structures and ΔG values for each electron transfer step are given in Tables 12 and 13.

FsTA experiments were performed on the **$NDI^{\cdot-}$-DPA-PhPy** ligand and the results are shown in Fig. 21. Analysis using multiple-wavelength global fitting revealed that the back-electron transfer step has a shorter lifetime (4.8 ps) than the forward-electron transfer step (27.3 ps). As a result, the spectral features of $DPA^{\cdot-}$ from 600 to 900 nm are not observed in the raw TA data (Fig. 21A) but do appear in the reconstructed species-associated spectra (Fig. 21B).

When the ligand is complexed with Re to form **NDI-DPA-PhPyRe(dmb)**, the fsTA and fsIR data shown in Figs. 22 and 23 are obtained. In this case, it proved impossible to fit a species in which the DPA is reduced, indicating that just as in the **$NDI^{\cdot-}$-DPA-Re(bpy)** complex the $DPA^{\cdot-} \rightarrow$ Re(bpy) electron

Table 12
Donor–acceptor distances in **NDI-DPA-PhPyRe(dmb)** calculated from the DFT-optimized geometries. Data taken from [52].

Moiety	Distance to Re (Å)
NDI	23.0
Anthracene	12.3
dmb	2.8

Table 13
Driving force for electron transfer reactions in **NDI-DPA-PhPy** and **NDI-DPA-PhPyRe (dmb)**. Data taken from [52].

Compound	Process	ΔG (eV)
NDI-DPA-PhPy	$^{*}NDI^{\cdot-} \rightarrow DPA$	−0.26
NDI-DPA-PhPy	$DPA^{\cdot-} \rightarrow NDI^{0}$	−1.34
NDI-DPA-PhPyRe(dmb)	$^{*}NDI^{\cdot-} \rightarrow DPA$	−0.27
NDI-DPA-PhPyRe(dmb)	$DPA^{\cdot-} \rightarrow dmb$	−0.76
NDI-DPA-PhPyRe(dmb)	$DPA^{\cdot-} \rightarrow NDI^{0}$	−1.33
NDI-DPA-PhPyRe(dmb)	$dmb^{\cdot-} \rightarrow NDI^{0}$	−0.57

transfer step is much faster than the 4.8 ps observed for $DPA^{\cdot-} \rightarrow NDI^{0}$. Back-electron transfer is slowed down dramatically in **$NDI^{\cdot-}$-DPA-PhPyRe(dmb)** compared to **Phbpy-Re-PyPhNDI$^{\cdot-}$**. Nanosecond TA shows that the NDI^{0} features and $NDI^{\cdot-}$ ground state bleaches decay via a combination of first-order and second-order kinetics. This indicates that the charge-separated state is sufficiently long-lived to enable molecular diffusion and intermolecular back-electron transfer. Fitting the kinetic trace to the differential equation

$$\frac{d[CS]}{dt} = -\left(\frac{1}{\tau_{BET2}}[CS] + \frac{1}{\tau_{IM}}[CS]^2\right) \quad (6)$$

where [CS] is the concentration of the charge-separated state, τ_{BET2} is the intramolecular back-electron transfer rate and τ_{IM} is the bimolecular charge transfer rate, we obtain the first order lifetime of τ_{BET2} = 43.4 μs for intramolecular back-electron transfer. This is a staggering improvement over the 29.7 ns lifetime obtained for back-electron transfer in the complex without the DPA intermediate acceptor, and the longest lifetime yet observed for a complex containing a radical anion chromophore. While this particular complex is not useful for catalysis due to the dissociation of the Py

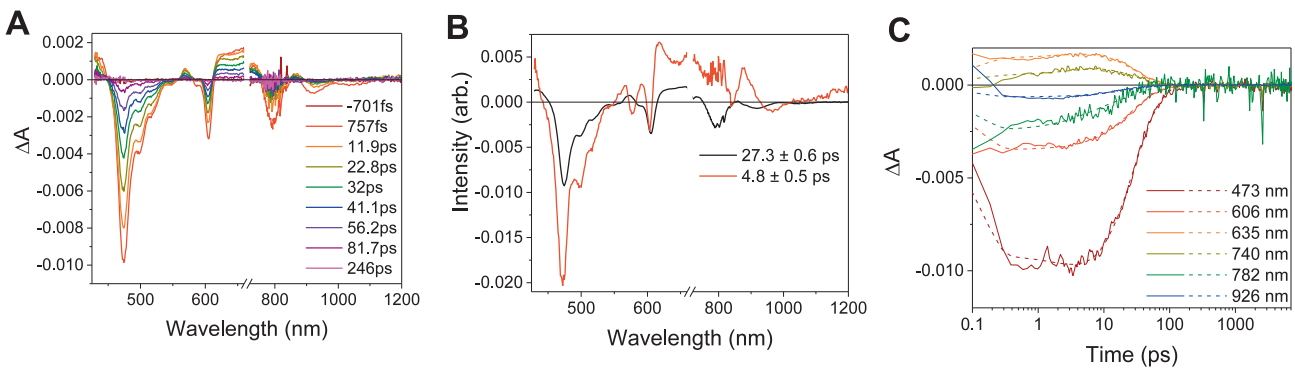

Fig. 21. Transient absorption data for **$NDI^{\cdot-}$-DPA-PhPy** in DMF (λ_{ex} = 700 nm) with excess TDAE added. (A) Transient absorption spectra; (B) Species-associated spectra; (C) multiple-wavelength kinetic traces and fits. Reproduced from [52] with permission from the Royal Society of Chemistry.

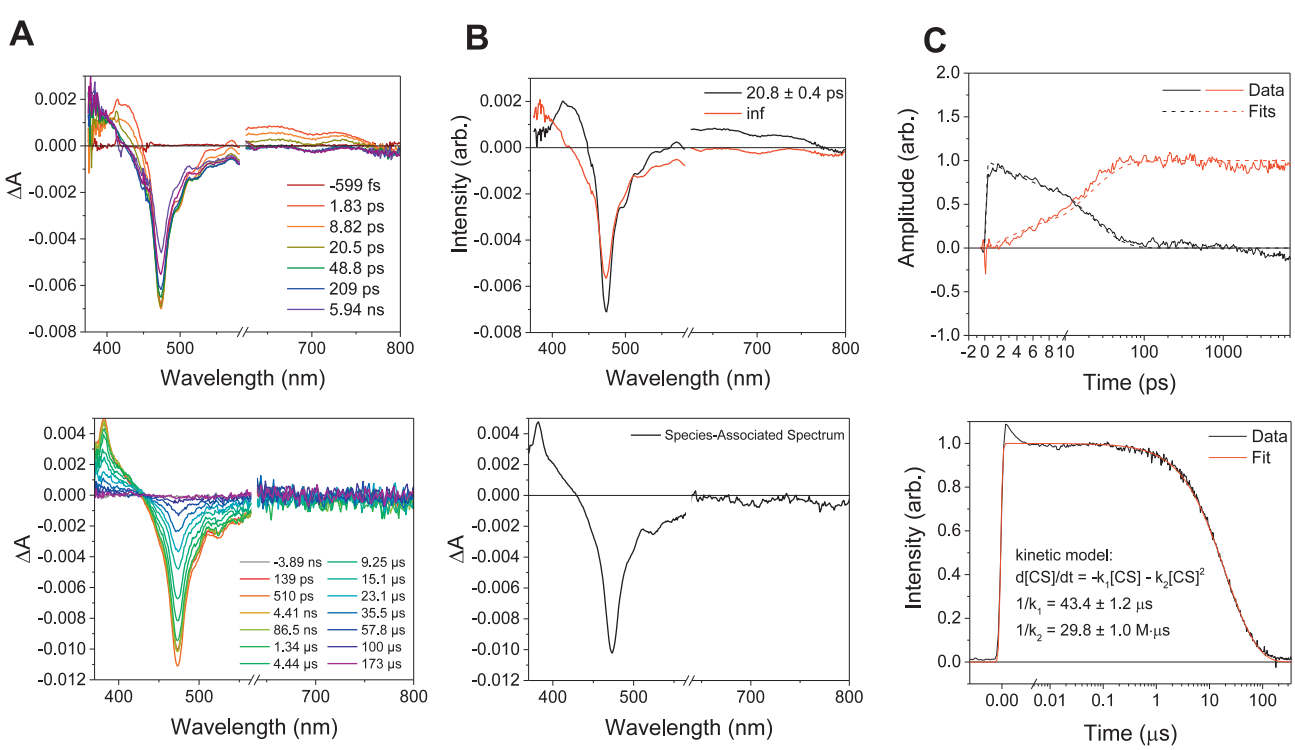

Fig. 22. Transient absorption spectra for **$NDI^{\cdot-}$-DPA-PhPyRe(dmb)** in DMF (λ_{ex} = 605 nm) with excess TDAE added. (A) Transient absorption spectra. (B) Species-associated spectra. (C) Singular value decomposition kinetic traces and fits to the kinetic data based on the species-associated fits and lifetimes shown. Reproduced from [52] with permission from the Royal Society of Chemistry.

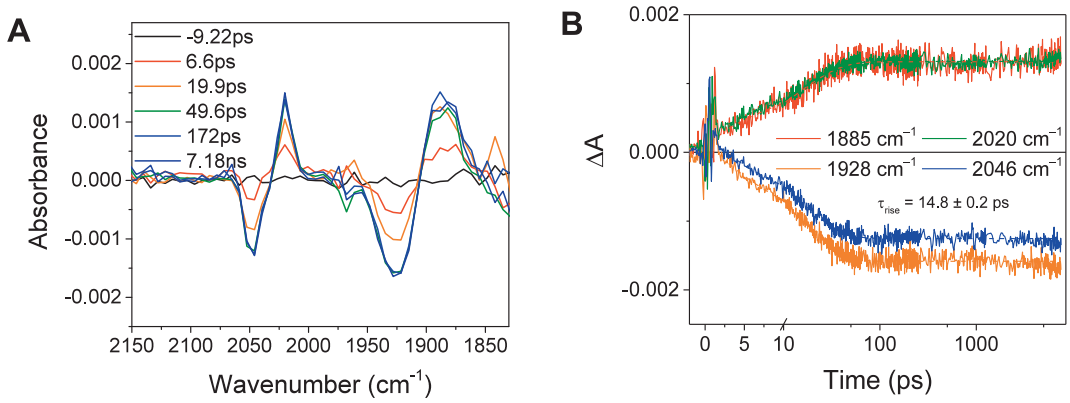

Fig. 23. (A) Time-resolved IR spectra and (B) global multiple-wavelength kinetic traces and fits for **NDI$^{\cdot-}$-DPA-PhPyRe(dmb)** in DMF (λ_{ex} = 605 nm) with excess TDAE added. Reproduced from [52] with permission from the Royal Society of Chemistry.

ligand during the catalytic cycle, many metal complexes exist with non-dissociating pyridine ligands for which the **NDI-DPA-Py** ligand could serve as a useful chromophoric ligand.

5. Systems in which Re-bpy MLCT is excited

5.1. PDI radical anion and triplet–triplet electron transfer

Up to this point, we have discussed RDI–Re dyads where the RDI anion functions both as a chromophore and an electron donor. However, it is also possible to separate the chromophore and electron donor functionalities by using the Re(bpy) MLCT transition as the chromophore, whose excited state is reductively quenched by the appended RDI anion. In this way, the RDI moiety provides the opportunity to perform photoelectrocatalysis at modest potentials, where the bulk of the driving force is provided by the incident photons. In addition, as will be discussed below, excitation of the Re → bpy MLCT offers the potential to use spin dynamics to dramatically lengthen the lifetime of the charge-separated state [41]. For this work, we focused on the **PDI-Phbpy-Re-Py** dyad initially discussed in Section 4.1.1 (Scheme 6).

Transient absorption data collected after excitation of the complex at 414 nm, shown in Fig. 26A, are quite a bit more complicated to interpret than those shown in Section 4.1.1, where the complex was excited at 705 nm or 950 nm. At 414 nm, excitation is exclusively into the broad Re → bpy MLCT band that peaks around 385 nm and tails into the visible region, however immediately after excitation, the ground-state absorptions of the PDI$^{\cdot-}$ moiety from 650 to 800 nm (Fig. 24B, black) are observed to bleach, while peaks at 525 nm, 485 nm, and 460 nm attributable to neutral,

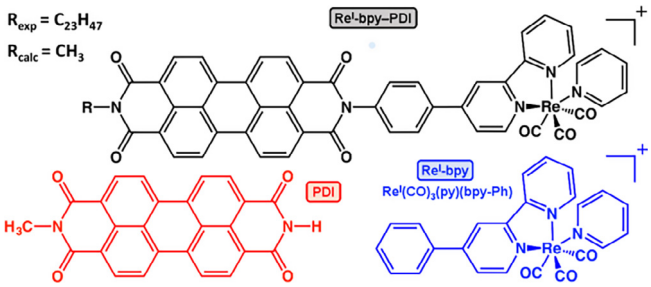

Scheme 6. Structure of the **PDI-Phbpy-Re-Py** dyad and the constituent **PDI** (red) and **Phbpy-Re-Py** (blue) molecules. The **Phbpy-Re-Py** complex bears a positive charge in its ground state, and the PDI in the dyad is chemically reduced before photoexcitation. Reproduced with permission from [41] Copyright 2017 American Chemical Society.

ground-state PDI^0 (Fig. 24B, blue) appear. In addition to those peaks, however, a broader absorption, centered at 505 nm, and a weak absorption tailing to 620 nm also appear. The weaker red absorption is attributable to Re(bpy$^{\cdot-}$)(CO)$_3$, while the broad 505 nm absorption is assigned on the basis of literature precedent [58,59] and TD-DFT calculations as the triplet excited state of neutral PDI (^{3*}PDI^0).

The PDI^0 peaks decay within 200 ps, while the ground state bleach decays to approximately half its initial intensity, but the ^{3*}PDI^0 peak and the remaining half of the bleach persist past the end of the 8 ns fsTA experiment. Nanosecond TA experiments show that these features have a lifetime of 67 ns. Femtosecond IR experiments show production of the Re(bpy$^{\cdot-}$)(CO)$_3$ state within the instrument response, and persistence of that state past the end of the 8 ns experimental window.

Two observations are key to explaining these results. First is that the singlet MLCT state (^{1}MLCT) produced upon excitation at 414 nm undergoes intersystem crossing to the triplet MLCT (^{3}MLCT) state within 150–200 fs [49,60–62]. The second is that while the coupling between the PDI and Re(bpy) moieties is minimal, it is nonzero. The result is that after excitation of the Re(bpy) fragment into a triplet state, the molecule contains two sets of unpaired electrons, one on the PDI fragment (S = ½) and one on the Re(bpy) fragment (S = 1). These two fragments can combine to form an overall quartet state (S = ½, shown in Fig. 25A, steps B1 and B2), or an overall doublet state (S = ½, shown in Fig. 25A, steps A1 and A2). This leads to a branching of the decay pathways.

These two spin states are isoenergetic due to the small electronic coupling. A conventional treatment of spin statistics such as that employed by Rugg et al. [63] would suggest that the two states are populated proportionate to their multiplicity, giving a 2:1 ratio of quartet to doublet. However, this treatment assumes that the triplet state is unpolarized. Intersystem crossing through spin–orbit coupling, as occurs in Re(bpy)(CO)$_3$L, is known to produce a spin-polarized triplet in which one triplet sublevel is populated with at least 90% selectivity [64,65]. When such as spin-polarized triplet encounters a doublet, the population of the two resultant spin states is dictated only by the spin polarization of the doublet. In this case, the two spin states of the PDI$^{\cdot-}$ doublet are equally populated, leading to an approximately equal population of the overall doublet and overall quartet states. Because of the spin polarization of the triplet after intersystem crossing, the Re(bpy) fragment in Fig. 27A can be seen as having two down spins in its triplet state, while the direction of the single unpaired spin on the PDI fragment determines the overall spin multiplicity of the system.

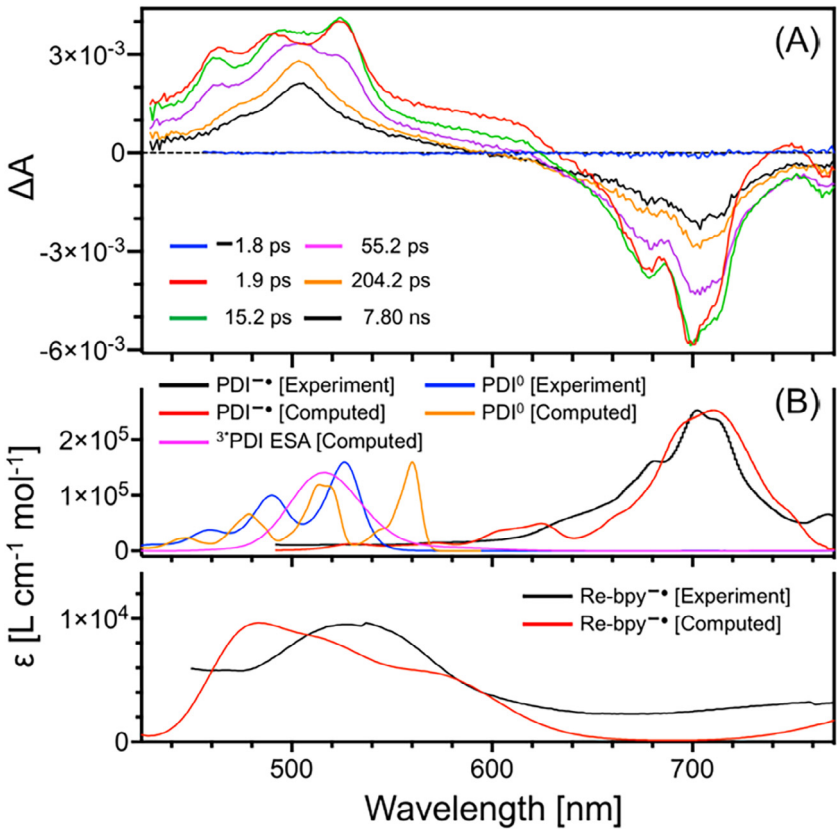

Fig. 24. (A) Transient absorption spectra of **PDI$^{\cdot-}$-Phbpy-Re-Py** pumped at 414 nm. (B) Vibronically resolved,[10] calculated absorption spectra for the $S_1 \leftarrow S_0$ electronic transition in PDI^0 and the three lowest-energy $D_n \leftarrow D_0$ transitions in PDI$^{\cdot-}$. Experimental and vertical absorption spectra of **Phbpy-Re-Py$^-$**. Reproduced with permission from Ref. [41] Copyright 2017 American Chemical Society.

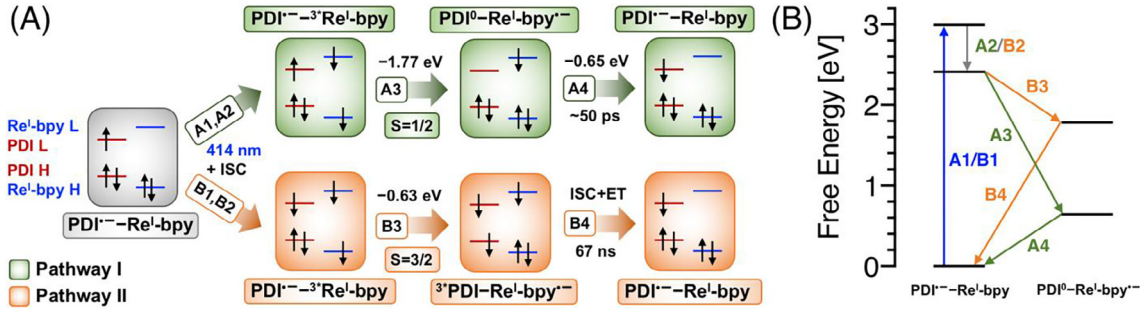

Fig. 25. (A) Orbital diagram of the low-spin (top) and high-spin (bottom) pathways as photoinduced by excitation at 414 nm. H = HOMO, L = LUMO. Note that the variation of orbital energies with electronic state is neglected in this schematic depiction. (B) Jablonski diagram with the x-axis representing the degree of charge shifting between PDI and Re(bpy). Adapted from [41]. Original copyright 2017 American Chemical Society.

The top pathway, where the overall spin state is a doublet, proceeds first by rapid electron transfer from the PDI LUMO to the Re (bpy) HOMO, generating the ground state of PDI^0 and the reduced Re(bpy$^{\cdot-}$) (Fig. 27A, step A3). As evidenced by the appearance of PDI^0 bands within the instrument response, this electron transfer is extremely rapid. At this point, back-electron transfer (Fig. 25A, step A4) is exothermic and proceeds with a lifetime of approximately 50 ps to regenerate the ground state. In the bottom pathway, where the overall spin state is a quartet, the first step is hole transfer from the Re(bpy) HOMO to the PDI HOMO, producing ^{3*}PDI^0 and reduced Re(bpy$^{\cdot-}$) (step B3). Unlike in the doublet pathway, however, back-electron transfer (Fig. 25A, step B4), while extremely exothermic, is spin-forbidden. It is for that reason that the quartet charge-separated state has such a long lifetime. The fsTA data support our conclusion regarding the relative populations of the doublet and quartet states after intersystem crossing; we observe an approximately 50% decrease in the intensity of the PDI$^{\cdot-}$ bleach feature at 204 ps (Fig. 24A, yellow trace), a time-point at which the CS state produced by the doublet pathway has returned to ground but the quartet pathway has barely decayed.

The process in step B3 involves the transfer of a triplet state from one moiety to another. However, this process is not the typical triplet–triplet energy transfer (TTEnT) process normally observed in cases where a triplet exciton moves from one moiety to another. TTEnT, a Dexter-type process, requires precise donor–acceptor energy matching to proceed, and step B3 is significantly exothermic. Instead, the process is a much-rarer triplet–triplet

electron transfer (TTET) process, whose rate can be computed using the Marcus equation for electron transfer. Because electron transfer to the ground state is spin-forbidden, electron transfer produces an electronically excited state in the acceptor moiety, in this case the triplet excited state of PDI.

The Jablonski diagram for the two pathways is shown in Fig. 25B. The Marcus parameters for each electron transfer process were calculated using a recently reported protocol [66] and using those parameters, theoretical rates were calculated using the Marcus equation and compared to the observed rates (Fig. 26). If the thermal average of the donor–-acceptor geometries is used to calculate the electronic couplings, the rates are severely underestimated. However, if the donor–acceptor geometries exhibiting the strongest coupling are used, the calculated rates are found to match quite closely. To justify the choice of using the strongest-coupling geometries, we observe that the ^{1}MLCT → ^{3}MLCT transition is exothermic by 0.6 eV, and that the extra energy associated with that intersystem crossing event takes approximately 10 ps to equilibrate to the solvent. The electron transfer steps A3 and B3 occur within only ~2 ps, before the donor–acceptor geometries can thermally equilibrate, increasing the rate of thermally activated electron transfer.

5.2. PDI dianion and formation of a triplet CS state

A very similar result to that observed in Section 5.1 is observed when the PDI moiety of **PDI-Phbpy-Re-Py** is reduced to the dianion. Upon excitation at 414 nm, the PDI^{2-} features bleach and induced absorptions of PDI$^{\bullet-}$ appear as shown in Fig. 27. These features decay with two time constants, 139 ns and 1.49 μs.

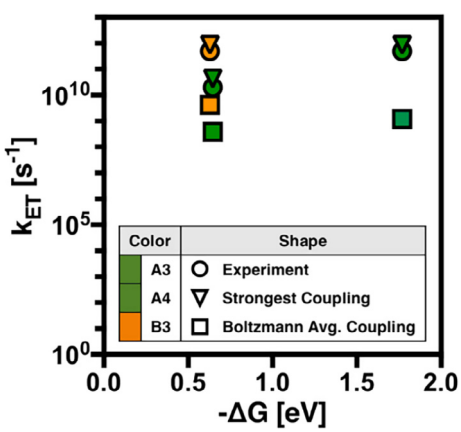

Fig. 26. ET rates as obtained experimentally from the transient absorption measurements and as calculated with Marcus theory using rotation-dependent electronic couplings either as Boltzmann-averaged over dihedral angles or as the point of maximum coupling. The −Δ*G* values from DFT are used for both calculated and experimental data points. Reproduced with permission from [41]. Copyright 2017 American Chemical Society.

Density functional theory (DFT) calculations were employed to elucidate the photoinduced electron-transfer mechanisms in **PDI^{2-}-Phbpy-Re-Py**. Fig. 28 shows a schematic orbital diagram with the involved states as triggered by a PDI-targeted 570 nm (Fig. 28C, see Section 4.1.1 for discussion of rates) or a Re(bpy) MLCT-targeted 414 nm pump pulse (Fig. 28A). The corresponding free energies are presented in Jablonski diagrams in Fig. 28D and B, respectively. The 570 nm pulse triggers a strongly allowed S2 ← S0 transition of the PDI^{2-} part. The excited electron then readily undergoes forward electron transfer (ET) since the calculated Δ*G* value is similar to typical ET reorganization energies for this system [41], making it near-activationless in the Marcus picture. Conversely, back-electron transfer is much slower due to a weaker exothermicity. This exothermicity is calculated to be −0.11 eV using DFT, although the value calculated using electrochemical data is −0.25 eV, as shown in Table 5. Errors of up to 0.2 eV are expected when performing DFT calculations of this nature.

Exciting the MLCT at 414 nm yields the S1 state which undergoes fast and quantitative intersystem-crossing (ISC) to the T1 state due to strong Re-induced spin–orbit coupling. In this case, swift reductive quenching from either the PDI^{2-} LUMO or HOMO yields the triplet charge-shifted state. The subsequent return to the resting state, in addition to lacking much driving force, is spin-forbidden, resulting in an extremely long-lived charge separation of >100 ns. We note that although the triplet and singlet charge-shifted states are degenerate to within <1 meV due to weak electronic coupling, they entail drastically different charge-recombination dynamics. These spin-dependent electron-transfer dynamics are somewhat analogous to those in the singly reduced dyad shown in Fig. 25. The distinction is that for the dianion, the entire excited-state population produces the high-spin charge-shifted state, whereas the same wavelength pump on the singly reduced dyad produced high- and low-spin charge-shifted states in equal amounts.

The observation of a long-lived charge-separated state whose lifetime is dependent on spin dynamics opens up the possibility of using molecular design to deliberately manipulate the spins of photocatalytic systems in order to achieve longer lifetimes. In addition to the long lifetimes of charge separated states observed in the two systems discussed above, it is worth pointing out that these are systems in which the MLCT excited state of Re(bpy)(CO)$_3$L is reductively quenched by a non-sacrificial electron donor. Many systems have been presented in the literature in which sacrificial reductive quenching of the excited state of Re(diimine)(CO)$_3$L leads to photocatalysis [13]. However, the sacrificial electron donors presented are not able to be regenerated. In this system, were photocatalysis to proceed, the PDI anion would not be regenerated by

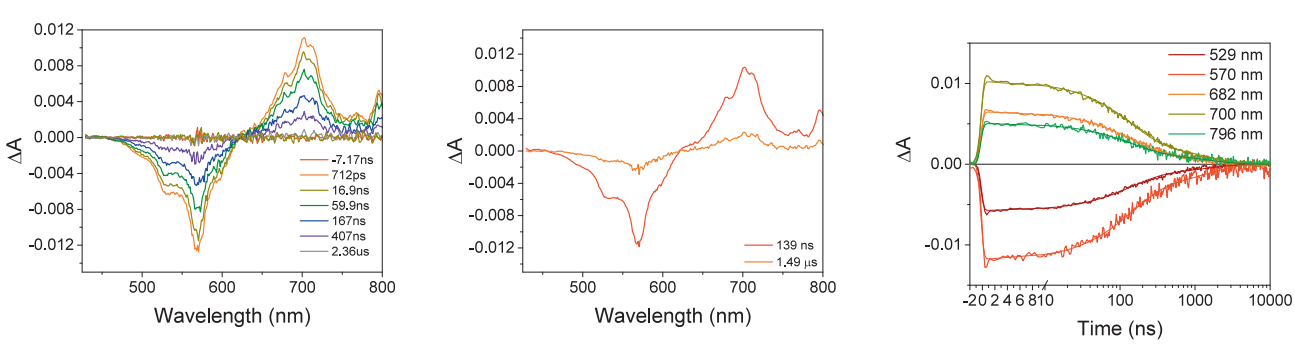

Fig. 27. *Left*: Transient absorption spectra of **PDI^{2-}-Phbpy-Re-Py** in DMF (λ_{ex} = 414 nm). *Center*: Species-associated spectra derived from multiple-wavelength fitting of the TA data. *Right*: Multiple-wavelength kinetic fits to the TA data.

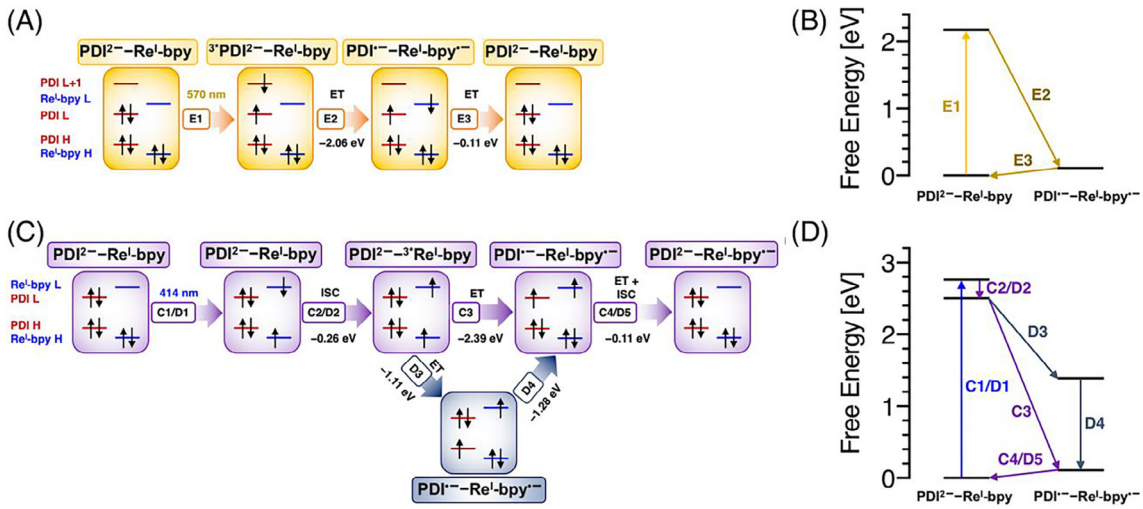

Fig. 28. (A) Schematic MO diagram of the photoinduced processes in **PDI^{2-}-Phbpy-Re-Py** resulting from a 570 nm optical pump. (B) Jablonski diagram with DFT-calculated free energies of the states depicted in panel A. (C) MO diagram of photoinduced processes in **PDI^{2-}-Phbpy-Re-Py** triggered by a 414 nm excitation. (D) Jablonski diagram of the states depicted in panel C.

back electron transfer. However, they could be regenerated electrochemically at potentials far positive of the potential required for electrocatalysis using the Re(bpy)(CO)$_3$L complexes. In effect, by exciting the complexes, they function as photoelectrocatalysts at a significant *under*potential, rather than the *over*potential that is typical of homogeneous molecular CO_2 reduction catalysts. Studies on complexes more suitable for catalysis are ongoing in our group. In the final section, our initial progress will be discussed and an outlook for the future presented.

6. Catalytic activity

We have performed experiments to demonstrate electrocatalytic activity. The complex chosen was **NDI-DPA-Re(bpy)**, discussed in Section 4.1.2, which was the bpy-linked complex that displayed the longest lifetime for the charge-separated state upon excitation of the RDI anion. Electrocatalytic activity was verified by comparing the cyclic voltammogram of the complex under Ar and under CO_2, as shown in Fig. 29. An increase in current was observed under CO_2 at the potential corresponding to the reduction of the Re center, as expected for an electrocatalyst [67]. We are currently in the process of developing a photoelectrochemical cell that utilizes the NDI radical anion and photo-driven multistep electron transfer to carry out CO_2 reduction.

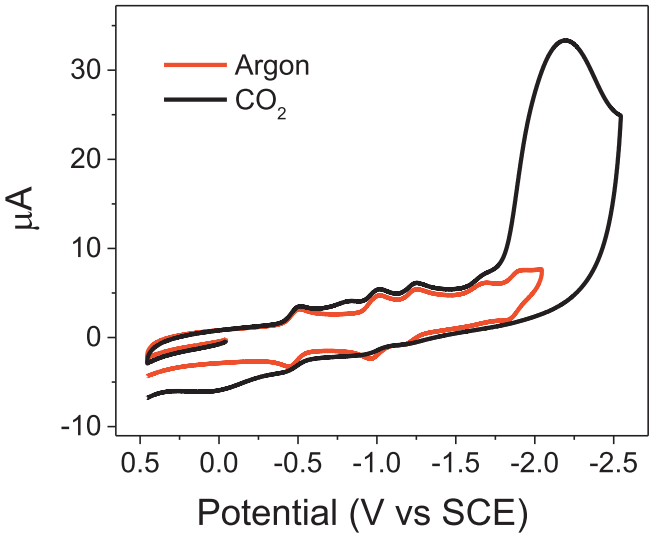

Fig. 29. Cyclic voltammograms of a 0.5 mM solution of complex 4 in 0.1 M $TBAPF_6$ in DMF under argon (red), saturated with CO_2 (black). Scan rate: 100 mV s^{-1}, glassy carbon electrode, Ag/AgCl reference electrode, platinum wire counter electrode. Reproduced with permission from [53].

7. Conclusion

The work described in this review has demonstrated that it is possible to attach rylenediimides to Re(bpy)(CO)$_3$L metal centers through a variety of geometries. It was demonstrated that attachment through the bpy ligand led to faster forward- and back-electron transfer rates as compared to attachment through an ancillary ligand, due to the bpy ligand being the site of reduction in the complex. We were successful in increasing the lifetime of the charge-separated state through several methods, either by incorporating an intermediate electron acceptor between the RDI anion and the Re(bpy)(CO)$_3$L complex, or by exciting the Re → bpy MLCT transition and depending on spin dynamics to prevent back-electron transfer. Our present efforts are focused on optimizing the metal center and connectivity to enable photoelectrocatalysis with these types of complexes. We are also exploring the possibility of sensitizing different metal centers, again with an eye towards achieving photoelectrocatalytic activity.

Acknowledgments

This work was supported by ANSER, an Energy Frontier Research Center funded by the U.S. DOE under Award No. DE-SC0001059 (experimental and computational work) and by a generous donation from the TomKat foundation (computational work). This publication was made possible by NPRP Grant No. 9-174-2-092 from the Qatar National Research Fund (a member of Qatar Foundation). Benjamin Rudshteyn performed preliminary calculations on the dianion dyad and Dr. Atanu Acharya supplied the pairwise Coulomb-interaction code. We thank Brandon Rugg and Dr. Elias Diesen for helpful discussions regarding the spin statistics of the **PDI-Phbpy-Re-Py** system discussed in Section 5.1. For computer resources, we thank Yale HPC, XSEDE, and NERSC.

Appendix A. Supplementary data

Supplementary data associated with this article can be found, in the online version, at https://doi.org/10.1016/j.ccr.2018.01.018.

References

[1] IPCC, Climate Change 2014: Synthesis Report. Contribution of Working Groups I, II and III to the Fifth Assessment Report of the Intergovernmental Panel on Climate Change, Geneva, Switzerland, 2014.
[2] N.S. Lewis, D.G. Nocera, Proc. Natl. Acad. Sci. U. S. A. 103 (2006) 15729–15735.
[3] National Renewable Energy Laboratory, Best Research-Cell Efficiencies. https://www.nrel.gov/pv/assets/images/efficiency-chart.png (accessed November 7, 2017).
[4] B. Kumar, M. Llorente, J. Froehlich, T. Dang, A. Sathrum, C.P. Kubiak, Annu. Rev. Phys. Chem. 63 (2012) 541–569.
[5] W. Sattler, L.M. Henling, J.R. Winkler, H.B. Gray, J. Am. Chem. Soc. 137 (2015) 1198–1205.
[6] W. Sattler, M.E. Ener, J.D. Blakemore, A.A. Rachford, P.J. LaBeaume, J.W. Thackeray, J.F. Cameron, J.R. Winkler, H.B. Gray, J. Am. Chem. Soc. 135 (2013) 10614–10617.
[7] S.B. Harkins, J.C. Peters, J. Am. Chem. Soc. 127 (2005) 2030–2031.
[8] M. Ruthkosky, F.N. Castellano, G.J. Meyer, Inorg. Chem. 35 (1996) 6406–6412.
[9] D.R. McMillin, M.T. Buckner, B.T. Ahn, Inorg. Chem. 16 (2002) 943–945.
[10] L. Flamigni, A. Barbieri, C. Sabatini, B. Ventura, F. Barigelletti, Photochemistry and photophysics of coordination compounds: iridium, in: Photochemistry and Photophysics of Coordination Compounds II, Springer Berlin Heidelberg, Berlin, Heidelberg, 2007, pp. 143–203.
[11] K.A. King, P.J. Spellane, R.J. Watts, J. Am. Chem. Soc. 107 (1985) 1431–1432.
[12] S.D. Cummings, R. Eisenberg, J. Am. Chem. Soc. 118 (1996) 1949–1960.
[13] H. Takeda, K. Koike, T. Morimoto, H. Inumaru, O. Ishitani, Photochemistry and photocatalysis of rhenium(I) diimine complexes, Elsevier Inc., 2011.
[14] E. Kato, H. Takeda, K. Koike, K. Ohkubo, O. Ishitani, Chem. Sci. 6 (2015) 3003–3012.
[15] Y. Kuramochi, O. Ishitani, Inorg. Chem. 55 (2016) 5702–5709.
[16] A. Gabrielsson, F. Hartl, H. Zhang, J.R. Lindsay Smith, M. Towrie, A. Vlček, R.N. Perutz, J. Am. Chem. Soc. 128 (2006) 4253–4266.
[17] Y. Tamaki, K. Koike, T. Morimoto, Y. Yamazaki, O. Ishitani, Inorg. Chem. 52 (2013) (1909) 11902–11909.
[18] D. Gosztola, M.P. Niemczyk, W. Svec, A.S. Lukas, M.R. Wasielewski, J. Phys. Chem. A 104 (2000) 6545–6551.
[19] E. Haviv, L.J.W. Shimon, R. Neumann, Chem. Eur. J. 23 (2017) 92–95.
[20] Y. Tamaki, K. Watanabe, K. Koike, H. Inoue, T. Morimoto, O. Ishitani, Faraday Discuss. 155 (2012) 115–127.
[21] K. Koike, S. Naito, S. Sato, Y. Tamaki, O. Ishitani, J. Photochem. Photobiol., A 207 (2009) 109–114.
[22] C.D. Windle, M.V. Campian, A.-K. Duhme-Klair, E.A. Gibson, R.N. Perutz, J. Schneider, Chem. Commun. 48 (2012) 8189–8191.
[23] C.D. Windle, R.N. Perutz, Coord. Chem. Rev. 256 (2012) 2562–2570.
[24] S. Sato, K. Koike, H. Inoue, O. Ishitani, Photochem. Photobiol. Sci. 6 (2007) 454–461.
[25] B.P. Sullivan, C.M. Bolinger, D. Conrad, W.J. Vining, T.J. Meyer, J. Chem. Soc., Chem. Commun. (1985) 1414–1416.
[26] F.P.A. Johnson, M.W. George, F. Hartl, J.J. Turner, Organometallics 15 (1996) 3374–3387.
[27] T. Morimoto, T. Nakajima, S. Sawa, R. Nakanishi, D. Imori, O. Ishitani, J. Am. Chem. Soc. 135 (2013) 16825–16828.
[28] E.E. Benson, M.D. Sampson, K.A. Grice, J.M. Smieja, J.D. Froehlich, D. Friebel, J.A. Keith, E.A. Carter, A. Nilsson, C.P. Kubiak, Angew. Chem., Int. Ed. 52 (2013) 4841–4844.
[29] A.S. Lukas, S.E. Miller, M.R. Wasielewski, J. Phys. Chem. B 104 (2000) 931–940.
[30] A.S. Lukas, P.J. Bushard, M.R. Wasielewski, J. Am. Chem. Soc. 123 (2001) 2440–2441.
[31] E. Shirman, A. Ustinov, N. Ben-Shitrit, H. Weissman, M.A. Iron, R. Cohen, B. Rybtchinski, J. Phys. Chem. B 112 (2008) 8855–8858.
[32] I. Ghosh, T. Ghosh, J.I. Bardagi, B. König, Science 346 (2014) 725–728.
[33] L. Zeng, T. Liu, C. He, D. Shi, F. Zhang, C. Duan, J. Am. Chem. Soc. 138 (2016) 3958–3961.
[34] M. Fujitsuka, S.S. Kim, C. Lu, S. Tojo, T. Majima, J. Phys. Chem. B 119 (2015) 7275–7282.
[35] C. Lu, M. Fujitsuka, A. Sugimoto, T. Majima, J. Phys. Chem. C 120 (2016) 12734–12741.
[36] C. Lu, M. Fujitsuka, A. Sugimoto, T. Majima, J. Phys. Chem. C 121 (2017) 4558–4563.
[37] A.D. Becke, J. Chem. Phys. 98 (1993) 5648–5652.
[38] F. Weigend, R. Ahlrichs, Phys. Chem. Chem. Phys. 7 (2005) 3297–3305.
[39] M.J. Frisch, G.W. Trucks, H.B. Schlegel, G.E. Scuseria, M.A. Robb, J.R. Cheeseman, G. Scalmani, V. Barone, B. Mennucci, G.A. Petersson, H. Nakatsuji, M. Caricato, X. Li, H.P. Hratchian, A.F. Izmaylov, J. Bloino, G. Zheng, J.L. Sonnenberg, M. Hada, M. Ehara, K. Toyota, R. Fukuda, J. Hasegawa, M. Ishida, T. Nakajima, Y. Honda, O. Kitao, H. Nakai, T. Vreven, J.A. Montgomery Jr., J.E. Peralta, F. Ogliaro, M. Bearpark, J.J. Heyd, E. Brothers, K.N. Kudin, V.N. Staroverov, R. Kobayashi, J. Normand, K. Raghavachari, A. Rendell, J.C. Burant, S.S. Iyengar, J. Tomasi, M. Cossi, N. Rega, N.J. Millam, M. Klene, J.E. Knox, J.B. Cross, V. Bakken, C. Adamo, J. Jaramillo, R. Gomperts, R.E. Stratmann, O. Yazyev, A.J. Austin, R. Cammi, C. Pomelli, J.W. Ochterski, R.L. Martin, K. Morokuma, V.G. Zakrzewski, G.A. Voth, P. Salvador, J.J. Dannenberg, S. Dapprich, A.D. Daniels, Ö. Farkas, J.B. Foresman, J.V. Ortiz, J. Cioslowski, D.J. Fox, F. Gaussian 09 Revision D.01, Gaussian, Inc., Wallingford CT, 2009.
[40] A.V. Marenich, C.J. Cramer, D.G. Truhlar, J. Phys. Chem. B 113 (2009) 6378–6396.
[41] S. Hedström, S. Chaudhuri, N.T. La Porte, B. Rudshteyn, J.F. Martinez, M.R. Wasielewski, V.S. Batista, J. Am. Chem. Soc. 139 (2017) 16466–16469.
[42] A.E. Reed, R.B. Weinstock, F. Weinhold, J. Chem. Phys. 83 (1985) 735–746.
[43] A. Viehbeck, M.J. Goldberg, C.A. Kovac, J. Electrochem. Soc. 137 (1990) 1460–1466.
[44] K.A. Grice, C.P. Kubiak, Recent studies of rhenium and manganese bipyridine carbonyl catalysts for the electrochemical reduction of CO_2, in: Inorganic Photochemistry, Elsevier Inc., 2014, pp. 163–188.
[45] J.A. Keith, K.A. Grice, C.P. Kubiak, E.A. Carter, J. Am. Chem. Soc. 135 (2013) 15823–15829.
[46] C.W. Machan, M.D. Sampson, S.A. Chabolla, T. Dang, C.P. Kubiak, Organometallics (2014), 140421073230005.
[47] N.T. La Porte, J.F. Martinez, S. Hedstrom, B. Rudshteyn, B.T. Phelan, C.M. Mauck, R.M. Young, V.S. Batista, M.R. Wasielewski, Chem. Sci. 8 (2017) 3821–3831.
[48] Y.F. Lee, J.R. Kirchhoff, R.M. Berger, D. Gosztola, J. Chem. Soc. Dalton Trans. 3677 (1995).
[49] A. Vlček, Ultrafast excited-state processes in Re(I) carbonyl-diimine complexes: from excitation to photochemistry, in: Photophysics of Organometallics, Springer Berlin Heidelberg, Berlin, Heidelberg, 2009, pp. 115–158.
[50] W. Kaim, S. Kohlmann, Chem. Rev. 29 (1990) 2909–2914.
[51] M.K. Kesharwani, B. Brauer, J.M.L. Martin, J. Phys. Chem. A 119 (2015) 1701–1714.
[52] M.R. Wasielewski, J. Martinez, N.T. La Porte, C.M. Mauck, Faraday Discuss. 198 (2017) 235–249.
[53] J.F. Martinez, N.T. La Porte, M.R. Wasielewski, J. Phys. Chem. C (2017), Just Accepted Manuscript.
[54] M. Médebielle, W.R. Dolbier Jr, J. Fluorine Chem. 129 (2008) 930–942.
[55] C. Burkholder, W.R. Dolbier, M. Medebielle, Tetrahedron Lett. 38 (1997) 821–824.
[56] N.G. Connelly, W.E. Geiger, Chem. Rev. 96 (1996) 877–910.
[57] E.R. Henry, J. Hofrichter, Singular value decomposition: application to analysis of experimental data, in: Methods Enzymol., Academic Press, 1992, pp. 129–192.
[58] V. Prusakova, C.E. McCusker, F.N. Castellano, Inorg. Chem. 51 (2012) 8589–8598.
[59] E.R.d. Santos, J. Pina, T. Venâncio, C. Serpa, J.M.G. Martinho, R.M. Carlos, J. Phys. Chem. C 120 (2016) 22831–22843.
[60] M. Busby, P. Matousek, M. Towrie, A. Vlček, J. Phys. Chem. A 109 (2005) 3000–3008.
[61] A. Cannizzo, A.M. Blanco-Rodríguez, A. El Nahhas, J. Šebera, S. Záliš, A. Vlček, M. Chergui, J. Am. Chem. Soc. 130 (2008) 8967–8974.
[62] A. El Nahhas, C. Consani, A.M. Blanco-Rodríguez, K.M. Lancaster, O. Braem, A. Cannizzo, M. Towrie, I.P. Clark, S. Záliš, M. Chergui, Antonín Vlček Jr., Inorg. Chem. 50 (2011) 2932–2943.
[63] B.K. Rugg, B.T. Phelan, N.E. Horwitz, R.M. Young, M.D. Krzyaniak, M.A. Ratner, M.R. Wasielewski, J. Am. Chem. Soc. 139 (2017) 15660–15663.
[64] W.S. Jenks, N.J. Turro, Tetrahedron Lett. 30 (1989) 4469–4472.
[65] M.S. de Groot, I.A.M. Hesselmann, J.H. van der Waals, Mol. Phys. 12 (1967) 259–264.
[66] S. Chaudhuri, S. Hedström, D.D. Méndez-Hernández, H.P. Hendrickson, K.A. Jung, J. Ho, V.S. Batista, J. Chem. Theory Comput. 13 (2017) 6000–6009.
[67] J.M. Smieja, C.P. Kubiak, Inorg. Chem. 49 (2010) 9283–9289.